



HAL
open science

P-T-t evolution of the Cycladic blueschist unit in Western Anatolia / Turkey: Geodynamic implications for the Aegean region

Mete Çetinkaplan, Osman Candan, Roland Oberhänsli, Masafumi Sudo,
Bénédicte Cenki-tok

► To cite this version:

Mete Çetinkaplan, Osman Candan, Roland Oberhänsli, Masafumi Sudo, Bénédicte Cenki-tok. P-T-t evolution of the Cycladic blueschist unit in Western Anatolia / Turkey: Geodynamic implications for the Aegean region. *Journal of Metamorphic Geology*, In press, 10.1111/JMG.12526 . hal-02460274

HAL Id: hal-02460274

<https://hal.umontpellier.fr/hal-02460274v1>

Submitted on 29 Jan 2020

HAL is a multi-disciplinary open access archive for the deposit and dissemination of scientific research documents, whether they are published or not. The documents may come from teaching and research institutions in France or abroad, or from public or private research centers.

L'archive ouverte pluridisciplinaire **HAL**, est destinée au dépôt et à la diffusion de documents scientifiques de niveau recherche, publiés ou non, émanant des établissements d'enseignement et de recherche français ou étrangers, des laboratoires publics ou privés.

Article type : Original Article

P-T-t EVOLUTION OF THE CYCLADIC BLUESCHIST UNIT IN WESTERN ANATOLIA / TURKEY: GEODYNAMIC IMPLICATIONS FOR THE AEGEAN REGION

Mete Çetinkaplan¹ Osman Candan¹ Roland Oberhänsli² Masafumi Sudo² Bénédicte Cenki-Tok^{3,4}

¹Dokuz Eylül Üniversitesi, Mühendislik Fakültesi, Jeoloji Mühendisliği Bölümü, 35160, Buca-İzmir, Turkey. e-mail: mete.cetinkaplan@deu.edu.tr

²Institut für Geowissenschaften, Universität Potsdam, Postfach 601553, 14415 Potsdam, Germany

³Laboratoire Géosciences Montpellier (CNRS-UMR 5243), Université de Montpellier, Place Eugène Bataillon, 34095 Montpellier Cedex France

⁴Earthbyte Research Group, School of Geosciences, University of Sydney, Sydney, NSW 2006, Australia

ABSTRACT

Eclogite and blueschist facies rocks occurring as a tectonic unit between the underlying Menderes Massif and the overlying Afyon Zone / Lycian Nappes and the Bornova Flysch Zone in western Anatolia represent the eastward continuation of the Cycladic Blueschist Unit in Turkey. This high-P unit is attributed to the closure of the Pindos Ocean and consists of (i) a Triassic to Upper Cretaceous coherent series derived from passive continental margin sediments and (ii) the tectonically overlying Upper Cretaceous Selçuk mélange with eclogite blocks embedded in a pelitic epidote-blueschist matrix. The coherent series has experienced epidote - blueschist facies metamorphism ($490 \pm 25^\circ\text{C}$ / 11.5 ± 1.5 kbar; 38 km depth). $^{40}\text{Ar}/^{39}\text{Ar}$ white mica and $^{206}\text{Pb}/^{238}\text{U}$ monazite dating of quartz metaconglomerate from coherent series yielded middle Eocene ages of 44 ± 0.3 and 40.1 ± 3.1 Ma for epidote-blueschist facies metamorphism, respectively. The epidote-blueschist facies metamorphism of the matrix of the Selçuk mélange culminates at $520 \pm 15^\circ\text{C}$ / 13 ± 1.5 kbar, 43 km depth, and is dated 57.5 ± 0.3 - 54.5 ± 0.1 Ma ($^{40}\text{Ar}/^{39}\text{Ar}$ phengite). Eclogite facies metamorphism of the blocks ($570 \pm 30^\circ\text{C}$ / 18 ± 2 kbar, 60 km depth) is early Eocene and dated at 56.2 ± 1.5 Ma by $^{206}\text{Pb}/^{238}\text{U}$ zircon. Eclogites experienced a nearly isothermal retrogression ($490 \pm 40^\circ\text{C}$ / $\sim 6-7$ kbar) during their incorporation into the Selçuk mélange. The retrograde overprints of the coherent series ($410 \pm 15^\circ\text{C}$ / 7 ± 1.5 kbar from Dilek Peninsula and $485 \pm 33^\circ\text{C}$ / $\sim 6-7$ kbar from Selçuk – Tire area) and the Selçuk mélange ($510 \pm 15^\circ\text{C}$ / 6 ± 1 kbar) are dated at 35.8 ± 0.5 - 34.3 ± 0.1 Ma by $^{40}\text{Ar}/^{39}\text{Ar}$ white mica and 31.6 ± 6.6 Ma by $^{206}\text{Pb}/^{238}\text{U}$ allanite dating methods, respectively. Regional geological constrains reveal that the contact between the Menderes Massif and the Cycladic Blueschist Unit originally formed a lithosphere-scale transform fault zone. $^{40}\text{Ar}/^{39}\text{Ar}$ white mica age from the contact indicates that the Cycladic Blueschist Unit and the Menderes Massif were tectonically juxtaposed under greenschist facies conditions during late Eocene, 35.1 ± 0.3 Ma.

This article has been accepted for publication and undergone full peer review but has not been through the copyediting, typesetting, pagination and proofreading process, which may lead to differences between this version and the [Version of Record](#). Please cite this article as [doi: 10.1111/JMG.12526](https://doi.org/10.1111/JMG.12526)

This article is protected by copyright. All rights reserved

Keywords: Cycladic Blueschist Unit, Menderes Massif, eclogite, Selçuk mélange, Pindos Ocean

1. INTRODUCTION

Blueschist and eclogite-facies rocks are significant markers of ancient zones of plate convergence and have been recognized commonly in Tethyan and Alpine-type orogenic belts. Late Cretaceous to Miocene high-pressure / low-temperature (HP/LT) rocks are common in the Aegean region and represent the subduction of oceanic crust and associated continental sediments during the closure of the Neo-Tethyan Ocean basin(s). Continental Greece and western Turkey are made up of a number of metamorphic and non-metamorphic tectonic zones as a consequence of Cretaceous to Miocene closure of these oceanic branches and following continental collision of continental blocks derived from both Laurussia and Gondwana. Mainland Greece is divided into two main tectonic zones, the Internal Hellenides to the north and the External Hellenides to the south (Faulp, Pavlopoulos, Klötzli, & Petrakakis, 2006; Papanikolaou, 2009, 2013 and references therein). The Internal Hellenides include, from northeast to southwest, the Rhodope Massif, Serbo-Macedonian Massif, Circum - Rhodope Zone, Vardar (Axios) Zone, Pelagonian Zone and the Cycladic high-P Unit. The Beotian, Parnassos-Ghiona, Pindos, Gavrovo-Tripolitza, Ionian and Paxos Zones belong to the External Hellenides (Figure 1a). In a general tectonic framework of western Anatolia, the Pontides (Sakarya and İstanbul zones) and Anatolides-Taurides form the main tectonic units and are separated by the E-W trending İzmir-Ankara-Erzincan suture (IAES) Zone representing the closure of the northern branch of Neo-Tethys (Okay & Tüysüz, 1999). The Anatolides represent the metamorphic equivalents of the Taurides (Candan, Çetinkaplan, Oberhänsli, Rimmelé, & Akal,

2005; Okay, Tansel, & Tüysüz, 2001) and consist of, from north to south, the Tavşanlı Zone, Afyon Zone / Lycian nappes and Menderes Massif (MM) (Figure 1a).

From bottom to top, the Cycladic high-P unit consists of two tectonic units. The Pre-Alpine basement (CB: Cycladic Basement; Flensburg, Stockli, Poulaki, & Soukis, 2019) is made of Neoproterozoic to Carboniferous metaclastics intruded by Variscan granites, which are related to the northward subduction of the Paleotethys under the Laurussia. The overlying Cycladic Blueschist Unit (CBU) can be divided into two sub-units; (a) coherent series consisting of Mesozoic passive continental margin sediments dominated by marbles with metapelite and rift-related early Mesozoic meta-basic / acidic volcanic interlayers deposited in the Pindos Ocean and overlying (b) meta-ophiolitic HP mélange (Syros-Selçuk mélange) (Flensburg et al., 2019; Okrusch & Bröcker, 1990). The CBU occurs as a tectonic unit sandwiched between the overlying Pelagonian Zone and underlying External Hellenides (Ring & Layer, 2003). The CBU is defined by Eocene (55-40 Ma, Forster & Lister, 2005; Tomaschek, Kennedy, Villa, Lagos, & Ballhaus, 2003) eclogite- to epidote-blueschist facies metamorphism (12-20 kbar / 450-550°C; Bröcker, Kreuzer, Matthews, & Okrusch, 1993; Schmädicke & Will, 2003) and Oligo-Miocene (ca. 25-16 Ma) regional greenschist facies overprint (4-9 kbar / 450-550°C, Bröcker et al., 1993; 5-7 kbar / 450-490°C, Ring, Will, Glodny, Kumerics, & Gessner, 2007). The MM is made of a poly-metamorphic (Candan et al., 2011b; Koralay, 2015) upper Neoproterozoic to lower Paleozoic basement (core series) and unconformably overlying Paleozoic to early Tertiary cover series (Özer, Sözbilir, Özkar, Toker, & Sarı, 2001). The cover series is dominated by Barrovian-type medium- to low-grade assemblages (Candan et al., 2011a; Cenki-Tok et al., 2015).

The eastward continuation of the CB/CBU towards western Anatolia and the relationship to the Paleogene metamorphic evolution of the MM is still unclear. The first petrological and geochronological data indicating an Eocene high-P metamorphism under blueschist to eclogite facies conditions in western Anatolia were reported by Candan, Dora, Oberhänsli, Oelsner, and Dürr (1997), Oberhänsli et al. (1998) and Ring, Laws, and Bernet (1999). The main outcrops of this high-P unit are exposed in the Selçuk - Dilek area and extend northeastwards up to Simav as discontinuous bodies (Candan et al., 2011a; Okay, 2001). The HP unit lays tectonically between the underlying MM and the overlying Lycian nappes / Bornova Flysch Zone (BFZ) (Rimmele, Jolivet, Oberhänsli, & Goffé, 2003; Ring et al., 2007) (Figure 1a-c). This high-P tectonic unit is

considered as extension the CBU in western Anatolia (Candan et al., 1997; Gessner, Ring, Passchier, & Güngör, 2001; Jolivet et al., 2010).

Here, we present the first detailed geological map of this eclogite-blueschist unit as well as petrographical descriptions and P-T quantification of the high-P rocks. Based on new petrological and geochronological data, we propose a geodynamic model for the P-T-t evolution of CBU in Turkey. Finally, we discuss the location of the CBU in western Anatolia and its structural relationship with the MM.

2. FIELD DESCRIPTIONS

2.1 The CBU

In western Anatolia, the CBU consists of two tectonic units; *i) Triassic (?) to Upper Cretaceous coherent series* and the tectonically overlying *ii) Selçuk mélange*. The coherent series is exposed in several localities from the Dilek Peninsula to Gölarmara (Figure 2 and Figure 3). It is made up of basal metaclastics and conformably overlying platform-type metacarbonates. The metaclastics are composed of chloritoid phyllite, mica schist, garnet-mica schist and metaconglomerate with blueschist facies metabasic layers. Based on the components, two types of metaconglomerate can be distinguished. The carbonate metaconglomerate contains elongated brownish to white marble pebbles embedded in a chlorite- and epidote-rich carbonate matrix and the quartz metaconglomerate consists of strongly flattened and elongated quartz pebbles in a quartz-rich sandy matrix. The quartz metaconglomerate contains Al-rich fine-grained silvery pelitic interlayers, up to one meter in thickness, which are characterized by ‘kyanite – chloritoid - phengite’ assemblages (Figure 4a). Chloritoid and kyanite occur as bow-tie- and rosetta-type porphyroblasts, up to 3 cm in size. Metabasite layers derived from basic volcanoclastics, from 10 cm to 5 meters in thickness, can be traced laterally up to 2 kilometers. The best outcrops are exposed in the Selçuk area and Dilek Peninsula (Figure 2 and Figure 3b). They are commonly intercalated with metaconglomerates and occur at the upper levels of the metapelite sequence. In the Dilek Peninsula, they contain well-preserved dark blue Na-amphibole needles in an epidote-rich matrix. In the northeastern part of the region, these rocks are almost completely retrogressed to greenschist facies metabasites. The existence of garnet-biotite schists NE of Selçuk suggest a

temperature increase during the retrogression of the coherent series from SW to NE of the CBU (Figure 1c and Figure 3a,b).

The metaclastics conformably grade into platform-type thick marbles. The transition zone is defined by an intercalation of yellowish dolomite, marble, quartzite and schist. The platform-type metacarbonates, (max. 2 km thick) are characterized by frequent metabauxite lenses at the lower levels. In the Dilek Peninsula and NW of Selçuk, metabauxites contain the assemblage diaspore – chloritoid. Towards the NE, they are rich-in corundum indicating the eastward increase of temperature during the Barrovian overprint (Candan et al., 1997). Based on well-preserved rudist fossils (Özer, 1993) a Late Cretaceous age can be assigned to the uppermost level of the platform-type metacarbonates.

The contact between platform carbonates and the overlying Selçuk mélange is a ductile shear zone (Figure 4b). The carbonates of the coherent series near Tire (Figure 3a), show grain-size reduction, strong flattening and the development of a foliation in massive marbles towards the contact. Metabasic rocks occurring at the base of the mélange exhibit gradual retrogression to greenschist facies. Chlorite and actinolite are present along the contact indicating that tectonic juxtaposition occurred under greenschist facies conditions. The Selçuk mélange crops out in four localities as discontinuous bodies between the Dilek Peninsula and Simav (Figure 1a). The main body (40 km long and 10 km wide) is exposed in the Selçuk area (Figure 2). It is characterized by a variety of high-P blocks in a garnet-phengite schist matrix. High-P blocks are made of eclogite, omphacite epidotite, omphacite metagabbro, blueschist metabasite and Ti-metagabbro. The Selçuk mélange contains serpentinites (up to 2 km wide x 3 km long) dolomite and marble blocks with metabauxite deposits (Figure 2). The blocks constitute ca. 20-25 % of the mélange. The matrix is dominated by garnet-phengite schist with subordinate albite-phengite-chlorite schist. However, due to an increase in temperature towards the NE, phengite and chlorite are replaced by muscovite and biotite as a consequence of Barrovian greenschist overprint (Figure 1c).

Eclogites have been recognized in numerous localities in Selçuk (Figure 2) and Gölarmara (Figure 3c). They occur as lens-shaped isolated bodies either in foliated serpentinites (Figure 4c) or in the metapelitic matrix. They are massive to weakly foliated rocks. Garnet porphyroblasts (up to 2-3 mm in size) sit in a groundmass of intergrown of omphacite (Figure 4d) and epidote. During

the lower amphibolite to greenschist facies overprint, the eclogite bodies were intensely deformed along their margins and within internal shear zones. Consequently, they show continuous mineralogical and textural changes, defined by an unaltered eclogitic core to a garnet amphibolite to greenschist metabasite rim. Serpentinite – eclogite contacts are characterized by up to 15 cm thick dark green metasomatic reaction zones consisting of chlorite and Ca-amphibole.

Omphacite epidotites are rare and have been recognized only in Söke, Selçuk and Torbalı. They occur as isolated bodies in serpentinite blocks, up to 3 meter in size. Omphacite epidotites (pseudo-eclogites) display patchy textures, which can be assigned to the former rodengitization of the gabbroic protoliths. They are massive to weakly foliated rocks characterized by the alignment of pale green omphacite and white to -green epidote crystals. Garnet occurs as euhedral small crystals (1-2 mm in size) and shows irregular local concentrations controlled by the heterogeneous bulk composition.

Omphacite metagabbros are coarse-grained rocks with a flaser texture. They occur as isolated blocks in the metapelitic matrix and as lens-shaped bodies embedded in serpentinites (Figure 4c). Although the original magmatic texture is well-preserved in the less-deformed cores of the bodies, primary plagioclase and clinopyroxene are completely replaced by clinozoisite and coarse-grained omphacite (Figure 4e). Along retrograde shear bands, omphacite is replaced by dark Ca-amphibole (edenite) and albite. Consequently, omphacite metagabbros have been transformed partly to completely into albite metagabbros.

The fine-grained greenschist metabasites, probably derived from a basaltic protolith, form the most dominant block type in the Selçuk mélange. They are massive to weakly foliated rocks, up to 1,5 km x 5 km in size, and consist predominantly of tremolite, chlorite and albite, with minor amounts of garnet. Their former blueschist mineral assemblage is rarely preserved and has been only recognized in two localities (Figure 2). Ti-metagabbro bodies, up to 300 m in length, are exposed north of Şirince (Figure 2). They are coarse-grained, titanite-rich (~ 10-15 vol. %), and dark colored rocks with a pronounced lineation defined by the alignment of Ca-amphiboles and titanite.

2.2 Contact relationships of the CBU with other tectonic units of western Anatolia

In western Anatolia the MM forms the lowest tectonic unit. The contact between the CBU and MM is a ductile thrust fault (Gessner et al., 2001). Although it extends from Dilek Peninsula to Simav, over more than 200 km, clear contact relations can only be observed in a few localities due to the presence of a widespread Neogene to Quaternary cover. South of Tire, where the contact is well exposed, the footwall is made up of high-grade, homogeneous garnet mica schists of the Precambrian basement of the MM. The coherent series of the CBU is exposed dominated by phyllites with thin marble layers. Contact relations were described in detail by Okay (2001). The regional Precambrian foliation of the garnet mica schists is progressively overprinted by penetrative shear bands within several tens of meters from the contact. They are defined by white mica and chlorite-rich zones after retrogression of biotite and garnet. This observation indicates that the MM and CBU were tectonically juxtaposed under greenschist facies conditions. West of Gölarmara, the contact between CBU and MM is also well exposed. The Selçuk mélange of the CBU rests on the low-grade Paleozoic cover series of the MM consisting of phyllite, quartzite and marble intercalations. Similar to the Tire area, the contact between the two units is characterized by a ductile shear zone defined by muscovite - chlorite phyllonites.

The CBU is tectonically overlain by both BFZ and the Afyon Zone / Lycian nappes. In the southwest of Gölarmara (Figure 3c) and east part of Gümüldür (Figure 3d), the BFZ forms the upper tectonic unit and consists of Mesozoic carbonate and ophiolite blocks embedded in an unmetamorphosed latest Cretaceous-Paleocene clastic matrix (Okay, İşintek, Altner, Özkan, Altner, & Okay, 2012). In Gümüldür, the BFZ rests on the Triassic section of the coherent series consisting of mica schists and conformably overlying metabauxite-bearing platform-type carbonates (Figure 1c). The contact is a brittle thrust fault defined by breccias that developed in carbonates from both units. In Gölarmara, the CBU consists of by the Selçuk mélange. Similar to Gümüldür, the contact is brittle, defined by fault breccias and gouge within a zone of up to 5 meter in thickness.

The Afyon zone and its southward transported equivalents (the Ören unit / Lycian nappes, Pourteau et al., 2013) form the other unit tectonically overlying the CBU. This Upper Cretaceous high-P unit consists of carpholite-bearing Triassic metapelites with metavolcanic layers and conformably overlying Triassic to Cretaceous aragonite marbles and Upper Cretaceous flysch (Candan et al., 2005; Pourteau et al., 2013). In the Söke - Kuşadası area, they occur as two klippen

resting on the Selçuk mélange (Figure 1c and Figure 2). The Triassic reddish phyllites with carpholite-chloritoid assemblage at the base of both klippen pass upwards into massive thick dolomites. Phyllites show an intense deformation at the base. Shear bands defined by chlorite, muscovite and retrogressed carpholites into pyrophyllite and kaolinite (Rimmelé, Oberhänsli, Candan, Goffé, & Jolivet, 2006) indicate the presence of a ductile shear contact formed under greenschist facies conditions. The contact relationships between the BFZ and the Afyon Zone/Lycian nappes is not observed in the Dilek – Selçuk area. However, it is described by Candan et al. (2016) in the Simav area where the Afyon Zone/Lycian nappes are tectonically overlain by the BFZ and the contact is represented by a brittle thrust fault.

3. PETROGRAPHY AND MINERAL CHEMISTRY OF HIGH-PRESSURE ROCKS

Petrographic studies are based on textural and mineralogical examination of >1000 thin sections. In total 16 samples (3 samples from the coherent series and 13 samples from the Selçuk mélange) were chosen for microprobe analysis. Analyses were performed on a JEOL8900 wavelength-dispersive automated electron microprobe at University of Mainz-Germany with LiF, PET and TAP analyzing crystals using natural and synthetic standards. Spot analyses were acquired with a 15-kV accelerating voltage, 5- μ m beam size, 15 nA beam current and counting times of 20s on peak and 10s on background. Amphibole nomenclature is based on Leake et al. (1997). The mineral abbreviations in this paper follow Whitney and Evans (2010). The general mineral assemblage of the investigated rocks and representative mineral analyses are given in Table 1 and Table 2-6, respectively.

3.1 Coherent series

Quartz metaconglomerate: It is made up of well-rounded quartz pebbles in a white mica-rich matrix. The matrix consists of kyanite + chloritoid + white mica \pm epidote \pm clinozoisite + chlorite + quartz + pyrophyllite + opaque oxide (Table 1). The modal amount of quartz in the matrix is greater than 50%. The high-P stage is represented by the mineral assemblage kyanite – chloritoid – phengite, which is restricted to Al-rich pelitic domains of the matrix (Figure 4a). Based on the textural relationships and Si values, two generations of white mica can be distinguished. Coarse-

grained phengites, which are aligned oblique to the main greenschist foliation have Si values ranging from 3.13 to 3.21 p.f.u. (Table 2a). The Mg+Fe²⁺ content of these phengites belonging to the prograde stage is quite low (0.08-0.23) with a composition close to the muscovite end-member (Figure 5a,b). Shear bands that developed during the greenschist overprint are defined by fine-grained muscovite (Figure 6a), chlorite and pyrophyllite. Si contents of this retrograde stage muscovites fall in the range of 3.04 - 3.08 p.f.u. (Table 2a; Figure 5a). In Si vs (Mg+Fe²⁺) diagram, white micas plot between muscovite and celadonite end-members representing ideal Tschermaks substitution (Figure 5b). Chloritoid porphyroblasts, up to 4 mm length, in the matrix display textural and compositional zoning. Mg# [Mg/(Mg+Fe)] value of chloritoid increases from core (0.27) to inner rim (0.35) (Table 3), whereas, a narrow fringe at the rim displays lower Mg# (0.28) and higher Mn contents, pointing to retrograde zonation of chloritoid.

Kyanite crystals are generally cloudy with fine-grained opaque oxide inclusions. The widespread presence of pressure shadows around chloritoid and kyanite porphyroblasts indicates that these porphyroblasts predate the formation of the retrograde matrix foliation. Kyanites are commonly replaced by fine-grained pyrophyllite (Figure 6b). Modal volume of epidote is <1%. Clinzoisite occurs in chloritoid as inclusions, whereas epidote is elongated and parallel to the retrograde foliation.

Blueschist and greenschist metabasites: the general mineral assemblage of metabasites consists of 'Na-, Na-Ca, Ca-amphibole + white mica + epidote + clinzoisite + albite + chlorite + titanite + calcite / ankerite + quartz + opaque oxide' (Table 1). Calcite mode reaches up to 35 vol. % in these volcanoclastic rocks. They show nematoblastic textures defined by parallel alignment of prismatic amphibole crystals. Na amphibole – phengite - epidote I - calcite - quartz - opaque oxide form the high-P assemblage. Si contents of white micas from prograde and retrograde stages are 3.35-3.44 p.f.u. and 3.14-3.16 p.f.u., respectively (Table 2a; Figure 5a,b). Na-amphiboles (Al^{VI}: 0.78-1.20 p.f.u.) plot in the glaucophane field (Figure 5c; Table 4). They are rimmed by barroisite (Al^{VI}: 0.34-0.53 p.f.u.; Figure 5d) or replaced by chlorite (X_{Mg} = 0.60-0.62). ^(B)Na and X_{Mg} (Mg/Mg+Fe) contents of glaucophane range between 1.85 – 1.89 and 0.53 – 0.58, respectively. These values range between 0.79 – 1.22 and 0.56 – 0.55 in the barroisitic rims (Figure 5d; Table 4). Ca-amphiboles after barroisite are tremolite – actinolite in composition. Representative epidote

analyses are given in Table 3. Pistacite contents of clinozoisite and epidote are 14-17 and 24-29 mol %, respectively. Plagioclases are rich-in albite (An_{4-5} mol %).

3.2 Selçuk mélange

Eclogite: the high-P mineral assemblage consists of omphacite, garnet, clinozoisite, rutile as well as apatite and zircon as accessory minerals (Figure 6c). Ca-amphibole, epidote, albite, quartz, titanite and chlorite are secondary minerals developed during the retrograde overprint (Table 1). In general, the eclogites show fine-grained granoblastic texture. In some samples, however, they may have a weak foliation defined by the alignment of omphacite and clinozoisite crystals. Omphacite occurs as prismatic crystals (up to 2 mm) or rarely they form rosetta-type clusters in massive rocks. Representative clinopyroxene analyses are given in Table 5. According to textural evidence, three types of clinopyroxene can be distinguished. Coarse-grained omphacite (Cpx-I) representing the high-P-stage displays a homogeneous composition (Jd_{32-45} - Ae_{8-13} - Q_{45-57} mol %) and plot in the omphacite field (Figure 7a). Fine-grained aggregates replacing coarse-grained omphacitic clinopyroxene (Cpx-II) is relatively poor-in jadeite (Jd_{23-25} - Ae_{6-8} - Q_{56-63} mol %) and shows a transition from the omphacite to the Quad field (Figure 7a). Clinopyroxene in albite - clinopyroxene symplectites (Cpx-III) is augitic in composition (Jd_{6-8} , Ae_{7-8} , Q_{84-87} mol %) and mainly plot in the Quad field (Figure 7a). The mode of epidote group minerals reaches up to 25 vol. % in the rocks. The pistacite end-member of the clinozoisite is 14-18 mol % (Table 3). Garnet forms idioblastic porphyroblasts, up to 2-3 mm, with a poikilitic texture (Figure 6c). Omphacite, clinozoisite, quartz and rutile inclusions in garnet can make up to 50 vol. % of the host mineral. Representative garnet compositions are plotted on the $Mg+Fe^{2+}$ - Mn - Ca diagram (Table 6; Figure 7b). Garnets are an almandine-spessartine solid solution with grossular and minor pyrope (3-8 mol%) components (Figure 8a). Growth zoning represented by the substitution of Fe^{2+} for Mn from core to rim commonly shows a characteristic Mn bell-shaped profile. This involves an increase in almandine (41-42 mol % in the core to 47 mol % in the rims) and a decrease of spessartine (from: 23-24 mol % to: 9-10 mol %) components (Figure 8a). X_{Grs} shows a more gradual increase towards the rims (from: 27-29 mol % to: 37-39 mol %). $Fe\#$ ($Fe^{2+}/(Mg+Fe^{2+})$) generally decreases from core to rim. In the outermost rim, the $Fe\#$ ratio displays an increase, representing the re-equilibration of rims with the matrix. Additionally, in some samples a pronounced oscillatory zoning from core to rim can be observed based on element distribution

maps of Mn, Ca and Fe (Figure 8b). In terms of Mn, three zones with reverse zoning can be distinguished (Figure 8b). Omphacite inclusions in garnet show a decrease in jadeite from core (Jd_{35}) to rim (Jd_{27}) (Figure 8b).

The retrograde overprint of eclogites is documented by the replacement of omphacite and garnet by amphibolite to greenschist facies mineral assemblages. In shear bands, omphacite is directly replaced by Ca-amphibole (actinolite / magnesio-hornblende) (Figure 5e). Whereas in the low-strain domains of the eclogitic bodies, omphacite is transformed first to fine-grained symplectitic intergrowths of clinopyroxene (Cpx-III) and albite (Figure 6d). It is then completely consumed by dark-green, medium to coarse-grained calcic-amphibole (edenite / magnesio-hastingsite) (Figure 5f) and albite. In general, garnet shows kelyphytic rims or is replaced by a greenschist facies assemblage of actinolite, epidote (Ps_{27} mol %), chlorite and albite. Rutile is rimmed by titanite coronas.

Omphacite epidotites: omphacite epidotite shows simple mineral composition consisting of epidote + clinozoisite (50-55 vol.%), omphacite (45-50 vol.%) and garnet (0-2 vol.%) (Figure 6e; Table 1). A weak foliation defined by the alignment of prismatic omphacite and clinozoisite crystals is noticed in thin sections. Clinozoisite is rimmed by thin epidote zones, which are probably related to the retrograde overprint. The pistacite ratio of the clinozoisite and epidote ranges between 13-18 % (Table 3) and 25-28 %, respectively. Euhedral small garnet crystals (1-2 mm) show an irregular distribution in the epidote-rich groundmass. In garnet-rich parts, omphacite epidotites have an eclogitic composition. Garnets show poikilitic textures with inclusions of omphacite and clinozoisite forming more than 40 vol.% of the host mineral. Similar to the eclogites, according to textural relations, omphacite can be divided into three groups as Cpx-I ($Jd_{38-40} - Ae_{10-13} - Q_{40-47}$ mol %), Cpx-II ($Jd_{34-36} - Ae_{8-17} - Q_{49-56}$ mol %) and Cpx-III ($Jd_{10-12} - Ae_{15-17} - Q_{68-71}$ mol %) (Figure 7a; Table 5). The retrograde overprint of omphacite epidotite is defined by the consumption of omphacite porphyroblasts (Cpx-I) by Na-poor clinopyroxene aggregates (Cpx-II), symplectites (Cpx-III) and Ca-amphibole (edenite and magnesio-hastingsite) (Figure 5f).

Omphacite metagabbro: the general mineral assemblage of omphacite metagabbros consists of 'clinopyroxene (I, II and III) + epidote + clinozoisite + Na-Ca amphibole (magnesiokatophorite) + Ca-amphibole (edenite) + rutile + titanite + albite + apatite + opaque oxide' (Table 1). Although

the original gabbroic texture can still be recognized, the primary igneous clinopyroxenes and plagioclase are completely replaced by omphacite and clinozoisite, respectively. Representative omphacite analyses are given in Table 5. Coarse-grained Cpx-I and clinozoisite (Ps₁₂₋₁₅ mol %, Table 3) form the preserved high-P assemblage of omphacite metagabbros. Furthermore, the presence of magnesiokatophorite (Na^(B)=0.66-0.68 p.f.u.; Figure 5g) points to the existence of former glaucophane in the high-P assemblage. At an early stage of retrogression, omphacite porphyroblasts (Cpx-I: Jd₄₀₋₄₂ mol %) were rimmed by the aggregates of recrystallized omphacite (Cpx-II: Jd₂₉₋₃₁ mol%) (Figure 6f). The symplectite assemblage consisting of Cpx-III (Jd₁₆₋₁₉ mol %) and albite is commonly derived from Cpx-II (Figure 6f; Table 5). In addition, clinopyroxene is replaced by edenite making more than 40 vol.% of the sample. These edenitic Ca-amphiboles are accompanied by epidote (Ps₂₆₋₂₈ mol %).

Blueschist and greenschist metabasites: the general mineral assemblage of the metabasites is 'Na-, Na-Ca-, Ca-amphibole + garnet + epidote + clinozoisite + chlorite + albite + titanite + quartz + opaque oxide' (Table 1). The high-P assemblage of the blueschist metabasites rarely preserved in low-strain domains and is represented by glaucophane, clinozoisite and garnet. Glaucophane (^(B)Na=1.64-1.85) occurs either as porphyroblasts in gabbroic metabasites or as inclusions in garnet with clinozoisite in fine-grained metabasalts. Porphyroblastic glaucophane is replaced by barroisite / winchite (^(B)Na=0.72-1.20) rims (Figure 5d and Figure 6g). Whereas, in the fine-grained greenschist metabasites, glaucophane in the groundmass was completely converted to tremolite / actinolite (^(B)Na=0.41-0.56) (Figure 5e; Table 4). In these rocks, garnet is resorbed by albite along the rims (Figure 6h). Garnet occurring as idioblastic porphyroblasts (up to 0.8 mm in size) shows almandine-spessartine solid solution, with moderate grossular (~17 - 23 mol %) and low pyrope (<10 mol %) contents (Figure 7b; Table 6). Garnet displays antithetic relations between spessartine (52_{core(c)} to 36_{rim(r)} mol %) and almandine (28_c to 42_r mol %) end-members. The Fe# decreases regularly from core to rim indicating one step growth zoning profiles (Figure 8c). Whereas, grossular (16_c – 18_r mol %) and pyrope (3_c – 5_r mol %) end-members display almost flat profiles (Figure 8c). A X-ray element distribution map of this garnet showing concentric zoning patterns parallel to the crystal faces is given in Figure 8d. Pistacite component of the clinozoisite in prograde stage ranges 16 - 17 mol % (Table 3). Retrograde mineral assemblage of Barrovian overprint in blueschist metabasites consists of actinolite, albite (An₁₋₂), epidote (Ps₂₉

mol %; Table 3), chlorite, titanite and quartz. Albite commonly forms poikilitic porphyroblasts, up to 1-1.5 millimeters, with inclusions of epidote, chlorite and titanite.

Matrix of Selçuk Mélange: garnet – phengite schists form the dominant lithology of the matrix of the Selçuk mélange and consist of ‘phengite + garnet + albite + chlorite + quartz + titanite + allanite + clinozoisite + opaque oxide’ (Table 1). They show lepidoblastic or porphyroblastic textures depending on the size and amount of garnet. Garnet displays textural zoning, defined by an inclusion-rich core including phengite (Si: 3.40 – 3.42 p.f.u.), clinozoisite (Ps₁₆ mol %) and quartz and an inclusion-poor rim. Representative garnet compositions are plotted on the Mg+Fe²⁺–Mn – Ca diagram (Table 6; Figure 7b). In this figure, garnet cores show Mn-rich compositions while the rims concentrate near the Mg+Fe²⁺-Ca corner of the triangle. Garnet is rich-in almandine (43_c - 65_r) with moderate grossular (27_c - 36_r mol %) and spessartine (28_c - 1_r mol %), and low pyrope (2_c - 6_r mol %) content (Figure 8e). It shows growth zoning with a bell shaped X_{Sps} distribution with almost an inverse pattern for X_{Alm} (Figure 8e). Two generations of white mica can be texturally recognized. Coarse-grained phengite of the high-P stage occurs generally in the matrix and as inclusions in garnet. It has high-Si contents ranging from 3.35 to 3.42 p.f.u. (Table 2a; Figure 5a,b). A compositional zoning which can be attributed to retrograde overprint is observed in phengite. This is documented by decreasing Si content from core (Si: 3.40 p.f.u.) to rim (Si: 3.24 p.f.u.). Fine-grained phengite, defining the main foliation of the matrix developed during the retrograde overprint is characterized by lower Si content (3.16 p.f.u.) (Table 2a). Albite porphyroblasts show a poikilitic texture due to inclusion of quartz and opaque. Garnet-biotite schist (Table 1) with low Si content (3.13 - 3.24 p.f.u.) –bearing phengite (Table 2a) is related with retrogression. Biotite, which is aligned parallel to the greenschist facies foliation of the matrix has X_{Mg}=0.54-0.55 and Al^{VI}=0.38-0.40 p.f.u.

4. P-T ESTIMATIONS

Metamorphic conditions for the CBU in western Anatolia were estimated by a combination of conventional thermobarometric calibrations based on exchange and net-transfer reactions and Theriak-Domino equilibrium assemblage calculations considering whole rock compositions and the

stable mineral assemblages. The estimated P-T conditions using conventional methods are given in Table 7.

4.1 Conventional thermobarometry

Fifteen representative samples from the coherent series and the Selçuk mélange were used to estimate the P-T conditions for high-P metamorphism and the lower amphibolite to greenschist facies overprint.

4.1.1 Selçuk mélange

Pelitic matrix: Fe-Mg exchange thermometry between garnet and muscovite was applied to two samples (94-30, M98-99/2) of the garnet – phengite schist with a mineral assemblage of garnet, phengite, albite and quartz. The calibration of Green and Hellman (1982) yielded temperatures of 503 – 540 °C for an assumed 13 kbar. The results are compatible with values from the Theriak-Domino modelling (see below). For the retrograde overprint estimations using the garnet-muscovite calibrations of Green and Hellman (1982), Wu, Wang, Yang, Geng, and Liu (2002) and Wu and Zhao (2006), temperatures range from 481 to 560°C for 6 kbar (Table 7).

Eclogite: Four samples (95-01, M98-45C, 95-21/10, SE-1) from three blocks were used to estimate the P-T conditions of the eclogite facies metamorphism. They are well preserved and homogeneous samples consisting of garnet in a groundmass of omphacite and epidote. X_{jd} of omphacite and X_{Fe} of garnet range between 21-44 mol % and 0.80-0.92 mol %, respectively. The thermometers of Ellis and Green (1979) and Krogh (1988) were applied to garnet - omphacite pairs. Compared with the temperature estimations (410-458°C) after Krogh (1988), the temperatures of Ellis and Green (1979) are ca. 70°C higher. They range between 531 and 617 °C for an assumed pressure of 18 kbar and are in reasonable concordance with the results Theriak-Domino modelling (see below). For the pressure estimation, the calibration of Holland (1980) yielded minimum pressure of 17.5 ± 3 kbar for an assumed temperature of 570°C. One sample from an amphibolitic rim of an eclogite block (M97-31) and two samples from slightly retrogressed eclogites (95-21/10 and M98-45C) were used to estimate the P-T conditions of the retrograde overprint. Calibration of Graham and Powell (1984) for garnet - amphibole pairs from these three samples yielded temperatures of 490°C to 545°C. Similarly, the Holland and Blundy (1994) calibration for amphibole - plagioclase pairs yielded the same range of temperature (507°C - 525°C). In these samples, plagioclase – hornblende – garnet –

quartz geobarometer (Kohn & Spear, 1989) yielded a pressure of 6.4 ± 0.5 kbar at an assumed temperature of 500°C indicating an isothermal decompression for lower amphibolite to greenschist facies overprint.

Omphacite metagabbros and omphacite epidotite: Due to the lack of garnet in omphacite metagabbro (91-16) only pressure estimations were performed. After calibration of Holland (1980), omphacite (Jd_{42}) yielded minimum pressures of 14 ± 0.3 kbar for assumed temperature of 530°C (Table 7). In omphacite epidotite (M97-151/3) for pairs of garnet (core) and omphacite (core), the garnet–clinopyroxene thermometer of Ellis and Green (1979) provides temperature estimations of $515\text{--}572^\circ\text{C}$ at 14 kbar. The calibration from Holland (1980) yielded minimum pressure of 14.2 ± 0.2 kbar at 560°C (Table 7).

Blueschist and greenschist metabasites: Two strongly retrogressed samples of blueschist metabasites with glaucophane and garnet (52/2 and 94-55/5) and one greenschist metabasite (M98-149/10) were used to estimate the conditions for the blueschist stage and greenschist facies overprint. The thermometric calibration of Graham and Powell (1984) for garnet – amphibole pairs yielded temperatures of $478 - 543^\circ\text{C}$ (52/2 and 94-55/5). P-T conditions for the retrograde stage were estimated using the net-transfer reaction for garnet + hornblende + plagioclase + quartz for barometer associated with the garnet – biotite exchange geothermometer. The Bhattacharya, Mohanty, Maji, & Sen (1992) calibration for garnet (rim) – biotite (matrix) pairs yielded a temperature of $479 - 496^\circ\text{C}$ (52/2). Using the Kohn and Spear (1989) geobarometer gave at pressure 6 ± 1 kbar for the retrograde overprint. For sample M98-149/10, which was completely retrogressed to greenschist facies, the Kohn and Spear (1989) geobarometer provided pressure estimates of 6.4 ± 0.5 kbar (Table 7).

4.1.2 Coherent series

Silica content of phengites in two garnet-mica schists (M99-52/5 and M97-36) ranges from 3.14 to 3.34 p.f.u. Based on white mica - garnet geothermometers (Green & Hellman, 1982 and Wu et al., 2002), temperature estimates for the epidote-blueschist facies and overprinting greenschist facies obtained from these samples are given in Table 7. Phengite (core) and garnet (inner rim) attributed to the high-P event yielded a range from 472 to 521°C for a pressure of 11 kbar (Table 7). Garnet (outer rim) and phengite (rim) pairs assigned to greenschist overprint using the Wu et al. (2002)

calibration gave temperature estimations between 490 – 518°C (Table 7). A temperature range of 452-483°C (M99-52/5) and 470-497°C (M97-36) (Table 7) for greenschist facies metamorphism from the Selçuk – Tire region was calculated using the distribution of Fe²⁺ and Mg between garnet (rim) and biotite (rim) based on the calibration of Bhattacharya et al. (1992) and Hodges and Spear (1982). The average estimated temperature for greenschist overprint in the Selçuk – Tire region is 485 ± 33°C. For the coherent series, pressure estimates for prograde and retrograde stages were performed based on the plagioclase / amphibole Al-Si partitioning (Molina, Moreno, Catro, Rodriguez, & Fershtater, 2015) for blueschist metabasite (90/11). Glaucophane (core) – plagioclase (core) pairs from the Dilek Peninsula yield pressures of 12 ± 2 kbar for epidote-blueschist facies, which are compatible with estimated values of the Theriak-Domino modelling (see below) (Table 7). In sample 90/11, actinolitic hornblende after glaucophane and plagioclase (rim) pairs gave a pressure of 7 ± 0.5 kbar attributed to greenschist overprint (Table 7). The garnet (rim) – plagioclase - muscovite (Si: 3.14 p.f.u.)-biotite (GPMB) geobarometer (Hodges & Crowley, 1985) yielded a pressure range of 5.9 – 7.6 kbar for the greenschist overprint of metapelites (M97-36, M99-52/5) (Table 7).

4.2 Theriak-Domino equilibrium assemblage diagrams

In addition to conventional P-T estimations, P-T equilibrium assemblage diagrams were calculated for one sample from the coherent series and five samples from the matrix and blocks of the Selçuk mélange (Figure 2 and Figure 3a,b). Thermodynamic calculations were performed using the Theriak-Domino software (de Capitani, 1994; de Capitani & Petrakakis, 2010) and the internally consistent and updated thermodynamic data set of Holland and Powell (1998; a modified version for Theriak-Domino software of the original ‘tc321p2.txt’ datafile of Thermocalc version 3.21). Mineral activity models are from Holland and Powell (1998). For the white mica-rich metapelitic matrix of mélange, calculation was performed in the Na₂O-CaO-K₂O-FeO-MgO-Al₂O₃-SiO₂-H₂O (NCKFMASH) system. For basaltic / gabbroic high-P blocks the Na₂O-CaO-FeO-MgO-Al₂O₃-SiO₂-H₂O (NCFMASH) system was used. In calculation of phase diagrams, epidote was used as a proxy for clinozoisite which contains only pure Al in its database composition. Therefore, we will use the terms ‘epidote-I’ and ‘epidote-II’ for clinozoisite (optically positive, monoclinic and iron-poor) and epidote (optically negative, monoclinic and iron-rich), respectively, in phase diagrams (Table 3). Bulk composition and Fe₂O_{3(T)} were measured by X-Ray Fluorescence Spectroscopy (XRF) (Table 8) in Potsdam University. The FeO was determined by wet chemical titration

(Appendix S2). $\text{Fe}_2\text{O}_{3(\text{T})}$ was recalculated accordingly. TiO_2 (in rutile), K_2O (in amphibole), MnO (in garnet) and P_2O_5 (in apatite) neglected.

Coherent series: The prograde assemblage in pelitic layers of quartz metaconglomerates from the Dilek Peninsula (D1) (Figure 3b) is defined by kyanite + chloritoid ($X_{\text{Mg}}=0.35$) + phengite + albite + epidote-I + quartz (Figure 9a). The stability field for this assemblage is defined by the absence of Prl, Grt, St, Lws, Omp and Fsp. Si isopleths of phengite were used to constrain the P-T condition of high-P stage. In sample D1, the maximum Si content of the phengitic white mica is 3.14 p.f.u. In the equilibrium assemblage diagram, P-T conditions for the high-P stage are 490 ± 25 °C and 11.5 ± 1.5 kbar (Figure 9a). These P-T conditions indicate a stability field at the low T side of the diaspore = corundum + H_2O reaction (Schmidt & Poli, 1994) in accordance with field observations (Figure 1c). In this sample, textural evidence shows that kyanite is partly or completely replaced by pyrophyllite during the retrograde overprint. The assemblage pyrophyllite + chloritoid ($X_{\text{Mg}}=0.28$) + white mica + albite + epidote-II + quartz occurring at the low temperature side of the pyrophyllite - kyanite univariant reaction represents the retrograde overprint of the high-P assemblage. P-T conditions for this stage can be constrained to 410 ± 15 °C and 7 ± 1.5 kbar by the Si isopleths (3.06 – 3.04 p.f.u.) of white mica in textural equilibrium with pyrophyllite for the Dilek Peninsula (Figure 9a).

Selçuk mélange: For the sample M98-99/2 (Figure 2) from the matrix of the mélange, the high-P stability field is defined by garnet + phengite + epidote + albite + chlorite (core) + quartz (Figure 9b). P-T conditions for the high-P stage are constrained to 520 ± 15 °C and 13 ± 1.5 kbar using of the maximum garnet X_{Prp} (0.04-0.06) and phengite Si (3.42 p.f.u.) isopleths. In the same P-T diagram, the assemblage albite + muscovite + chlorite representing the retrograde stage is constrained by the epidote- and garnet-out reactions. Using white mica (Si: 3.16 – 3.24 p.f.u.) and chlorite (rim) X_{Mg} (0.22 mol %) isopleths, P-T conditions were estimated at 510 ± 15 °C and 6 ± 1 kbar for the retrograde overprint (Figure 9b).

The high-P assemblage of eclogites is represented by the assemblage garnet + omphacite + epidote-I. The P-T equilibrium assemblage diagram of a representative sample (M98-45C) (Figure 2) is given in Figure 9c. In this diagram, the stability field of the high-P assemblage is constrained by X_{Alm} (0.50-0.54), X_{Prp} (0.06-0.08), omphacite ($X_{\text{Mg}}=0.7$) isopleths. The lawsonite- and

glaucophane-out reactions lie in a temperature – pressure range of 570 ± 30 °C and 18 ± 2 kbar. The mineral assemblage of the retrograde overprint is albite + epidote-II + pargasite + chlorite. Considering chlorite X_{Fe} (0,56) isopleths in the field of this assemblage, P-T conditions of this stage can be estimated at 490 ± 30 °C / 6 ± 1 kbar. For omphacite metagabbros (M98-50/1) (Figure 2), the stability field for the high-P assemblage omphacite (Jd_{40-42}) + epidote-I + glaucophane is defined by the garnet- and albite-out stability fields (Figure 9d). P-T conditions for the high-P-stage are 515 ± 60 °C and 15 ± 3 kbar. Glaucophane is present in the modelled high pressure assemblage, but not in the rock. However, the occurrence of magnesiokatophorite indicates that glaucophane was probably present during the high pressure stage. The stability field of the assemblage omphacite (Jd_{16-19}) + albite + epidote-II + Ca-amphibole indicates P-T conditions of 485 ± 40 °C and 6-7 kbar for the retrograde overprint of omphacite metagabbros. Omphacite epidotites are characterized by high modal amounts of epidote (mode >50%) and a patchy distribution of garnets. The stability field for the high-P assemblage, omphacite + epidote-I + garnet + quartz, covers a large area and is constrained by the absence of lawsonite-, glaucophane-, paragonite- and feldspar (Figure 9e). To estimate the P–T conditions of high-pressure metamorphism for sample M97-151/3 (Figure 2), the intersection isopleths of jadeite in omphacite (0.44–0.46) and X_{Mg} (0.06–0.08) of garnet (core and inner rim) were used (Figure 9e). Isopleth intersections show that omphacite and epidote-I are stable at temperature of 560 ± 40 °C and pressure of 16 ± 4 kbar during the high-P stage. The retrograde overprint is represented by omphacite (Jd_{11}) + epidote-II + chlorite + albite + Ca-amphibole (Figure 9e). The stability field of this assemblage is constrained by the absence of garnet and Jd_{10} isopleth of omphacite. These limitations give P-T conditions of 510 ± 30 °C / 6.5 ± 1.5 kbar indicating an isothermal decompression during the retrogression. An equilibrium assemblage diagram of the strongly retrogressed blueschist sample (52/2) (Figure 2) is illustrated in Figure 9f. In this diagram, the stability field of the high-P assemblage is restricted by garnet (inner rim) X_{Alm} (0.58-0.56) isopleths and lawsonite-, omphacite and chlorite-out fields. It yielded a P-T range of 525 ± 35 °C / 13 ± 0.5 kbar for the assemblage of garnet + glaucophane + epidote-I + albite + quartz. The mineral assemblage of upper greenschist retrograde overprint is actinolite + chlorite + epidote-II + albite + quartz. Considering the chlorite X_{Mg} (0.68-0.72) isopleths in the field of this assemblage, P-T conditions of this stage can be estimated at 505 ± 15 °C and 6 ± 1 kbar.

5. GEOCHRONOLOGY

Sample preparation and analytical techniques of Ar-Ar and U-Pb geochronology are given as supporting information (Appendix S1). The dated samples are described in Table 9. Sample locations are marked on Figure 2 and Figure 3a,b. The sample 122/1 is located out of mapping area (GPS coordinate: 35S 0559074/4210995).

5.1 $^{40}\text{Ar}/^{39}\text{Ar}$ Geochronology

$^{40}\text{Ar}/^{39}\text{Ar}$ spectra of the samples are shown in Figure 10. Results of the Ar isotope analyses and J values are given in the Table S1. Plateau ages were calculated for series of adjacent steps that represent individually more than 3%, and in all more than 50 % of the total ^{39}Ar release with more than three steps, and any of two steps in the plateau agree within 2 sigma error limits as following Fleck et al. (1977) and McDougall and Harrison (1999). Six of seven Ar analyses yielded well-defined age plateaus that represent 85–98 % of the total ^{39}Ar released.

In the coherent series of the CBU, we have dated three samples from the quartz metaconglomerate from the Dilek Peninsula (120/8, 123) and Selçuk (154/2), one sample from the contact between the CBU and the MM (122/1) east of Selçuk and one sample from a garnet-biotite schist (127/4) located in the Tire region.

White micas from the Dilek Peninsula and Selçuk yielded plateau ages of 35.8 ± 0.5 Ma for sample 120/8 (seven of eight steps; 98.0 % of the total ^{39}Ar ; Figure 10a), and 34.6 ± 0.1 Ma for sample 154/2 (8 of 9 steps; 97.3 % of the total ^{39}Ar ; Figure 10c), respectively. The analysis of sample 123 from the Dilek Peninsula did not yield a plateau age (Figure 10b), therefore, the total gas age or the isochron ages with all steps shall be considered. However, this sample shows 10 to 100 times anomalously enriched Ca-derived ^{37}Ar only in the lower temperature steps until step 6 although this was not found from any other white mica samples in this study. This suggests that the results of the age spectrum might reflect the mixture of Ar from the white mica and that Ca-bearing phase or materials. Steps from 7 to 9 are not defined as plateau steps, but show three similar ages which do not agree within two but within three sigma error. They show lower Ca contents than the previous steps and cover totally 53.2 % of total ^{39}Ar released. Therefore, we have calculated a weighted mean, 44 ± 0.3 Ma, from these three steps as equivalent to a plateau age. This age also agrees with the normal (Figure S1a) and inverse (Figure S1b) isochron ages, 43.2 ± 0.5 Ma and 44.2 ± 0.4 Ma, respectively, calculated from these three steps, both with the

initial atmospheric $^{40}\text{Ar}/^{36}\text{Ar}$ ratios within error. Therefore, these isochrons support that the weighted mean age is meaningful compared to the initial atmospheric Ar isotope ratios for those three steps. We conclude that the age for sample 123 is 44 ± 0.3 Ma. The sample (122/1) from the contact gives a plateau age of 35.1 ± 0.3 Ma (Figure 10d) from 6 of 9 steps; 85.4 % of the total ^{39}Ar . Additionally, a plateau age of 34.3 ± 0.1 Ma from garnet-biotite schist (127/4; Tire area) was obtained from 7 of the 10 heating steps corresponding to 92.7 % of total ^{39}Ar released (Figure 10e).

In the Selçuk mélange, phengitic white micas from two samples of garnet-phengite schists (M98-100/3 and 12-142) were dated. Sample M98-100/3 yielded a well-defined plateau age of 57.5 ± 0.3 Ma calculated for seven steps, representing 91.4 % of total ^{39}Ar released (Figure 10f). A similar plateau age of 54.5 ± 0.1 Ma was obtained from seven steps representing 94.9 % of the total ^{39}Ar released, from sample 12-142 (Figure 10g). All plateau ages presented here agree with all their isochron ages calculated from the plateau steps only except two inverse isochron ages from sample 12-154/2 and 12-127/4 because of relatively poorer precision and accuracy for the low intensities of ^{36}Ar (Table S1). As the isochron ages have larger errors than their plateau ages in all cases, we have preferred the plateau ages for the following discussion.

5. 2 U-Pb Geochronology

In the Selçuk mélange, one sample from a fresh eclogite (TR1620) and one sample from the pelitic matrix (112/1) were dated. Twenty-eight analyses in cores and rims of zircons from eclogite were performed (Figure 11a,b; Table S2). Seventeen points are concordant or sub-concordant between 450 and 50 Ma (Figure 11a). Three clusters of points can be noticed at ca. 450 Ma (Ordovician, Figure 11a), 320-300 Ma (Carboniferous, Figure 11c) and 240-190 Ma (Triassic, Figure 11d). Considering the evolution of the Tethyan region, they can be interpreted as the inherited zircons, which can be assigned to the rifting stage of the Paleotethys (von Raumer, Bussy, Schaltegger, Schulz, & Stampfli, 2013), Variscan event (Okay & Topuz, 2018) and Triassic rifting and opening of the new oceans (Pindos, Meliata etc.) on the southern margin of Laurussia (Stampfli & Borel, 2002), respectively. One single spot performed on a zircon rim yielded a sub-concordant Paleocene age with a $^{206}\text{Pb}/^{238}\text{U}$ apparent age of 56.2 ± 1.5 Ma (Figure 11e). This age at the Paleocene – Eocene transition is in good agreement with the white mica ages for HP metamorphism obtained from the Selçuk region and the Cyclades. This zircon grain shows a core

that is Cretaceous with a $^{206}\text{Pb}/^{238}\text{U}$ apparent age of 85.9 ± 2.1 Ma (Figure 11e). Considering the documented Cretaceous crystallization ages of the magmatic rocks (Bröcker, Löwen, & Rodionov, 2014; Tomaschek et al., 2003) from the Cyclades, it can be considered as the protolith age of the Selçuk eclogites.

Twenty-two rasters in allanite cores from the garnet-phengite schist from the matrix of the mélange (112/1) were performed. The data is represented in a Tera Wasserburg diagram (Figure 11f; Table S3) and yielded a lower intercept age of 31.6 ± 6.6 Ma (MSWD = 0.25). The low MSWD indicates that there is only one single allanite population. The $^{207}\text{Pb}/^{206}\text{Pb}$ y-intercept (0.8275) is in agreement with the value given by Stacey and Kramers (1976) for this age. Allanite is elongated parallel to the foliation (Figure 11g-i) and developed during the retrograde deformation.

In the coherent series, fifteen spots analyses on monazite grains from a quartz metaconglomerate (TR1610) were performed. Analyses are represented on the Concordia Diagram on Figure 12a (Table S4). This population yielded a lower intercept age of 34.1 ± 4.2 Ma (MSWD = 2.5). As data are not concordant, the weighted average of $^{206}\text{Pb}/^{238}\text{U}$ apparent ages for each spot were calculated (Figure 12b) and yielded 40.1 ± 3.1 Ma (MSWD = 2.5). Monazite grains are small (< 200 μm in size) and may be elongated in the foliation or rounded in the matrix made up of micas and quartz (Figure 12c,d).

6. DISCUSSION

Greece and western Anatolia are made up of several tectonic zones. A similar continuous southward younging trend of their medium- to high-P Alpine tectono-metamorphic evolutions is displayed in both Greece (Menant, Jolivet, & Vrielynck, 2016; Ring & Layer, 2003 and reference therein) and western Anatolia (Candan et al., 2005; Okay, Satır, Tüysüz, Akyüz, & Chen, 2001; Pourteau, Oberhänsli, Candan, Barrier, & Vrielynck, 2016 and reference therein). However, the E-W continuation and correlation of these zones remains controversial (Jolivet, Rimmele, Oberhänsli, Goffé, & Candan, 2004; Pourteau et al., 2013, 2016; Ring et al., 1999; Roche, Conand, Jolivet, & Augier, 2018). In this context, the study area is unique and is of special interest with respect to the contact relationship between some of these zones, especially the CBU and the underlying MM.

6.1 Eastward continuity of the CBU in western Anatolia

The Paleogene tectono-metamorphic evolutions of the CBU and the MM display considerable differences. The CBU is characterized by well-preserved Eocene (ca. 55 - 40 Ma) eclogite to blueschist facies metamorphism and following Oligo-Miocene (ca. 35-20 Ma) medium-P overprint, which are attributed to the closure of the Pindos Ocean (Bonneau, 1984; Jolivet & Brun 2010; Laurent et al., 2018; Philippon, Brun, & Gueydan, 2012). On the other hand, the Paleogene event in the MM is represented by typical medium-P Barrovian-type metamorphism attributed to burial beneath the southward-advancing Lycian nappes / Afyon Zone and the overlying oceanic slab (Candan et al., 2011a; Şengör & Yılmaz 1981 and references therein). The discovery of Eocene eclogite to blueschist facies rocks (Candan et al., 1997; Oberhänsli et al., 1998) in the Selçuk area led to exclude this region from the MM. Therefore, these rocks were interpreted as the eastward continuation of the CBU in western Anatolia (Candan et al., 1997; Gessner et al., 2001; Okay, 2001). More recently, a carpholite - chloritoid - kyanite assemblage occurring in Triassic metaconglomerates of a Mesozoic coherent series (Kurudere - Nebiler unit after Pourteau et al., 2013) along the southern flank of the MM was documented by Rimmele et al. (2003). It was interpreted as an evidence of a former high-P event (10–12 kbar / 440 °C) affecting the MM during its polyphase Alpine evolution (Rimmele et al., 2003). This high-P event was dated as Eocene by Ar-Ar geochronology, ca. 45 Ma (Pourteau et al., 2013). Considering the age similarities, this Mesozoic section was correlated with the CBU by Pourteau et al. (2013) following Ring et al. (1999) and Whitney, Teyssier, Kruckenberg, Morgan, and Iredale (2008). However, as stated by Jolivet et al. (2013), because of some stratigraphic and petrological discrepancies such as the apparent lack of carpholite in the CBU and eclogite and glaucophane in the Kurudere - Nebiler unit, this correlation is still open to discussion.

Recent detailed mapping of the southern flank of the MM (Alan et al., 2019; and unpublished fossil data; I. Alan, pers. com., 2019) revealed that the carpholite-bearing Triassic to Upper Cretaceous series is unconformably underlain by Upper Permian marbles with well-preserved fossils (*Mizzia* sp., *Bellerophone* sp., Fusulinid etc.) in many localities. Platform-type Upper Permian carbonates are regarded as a guide horizon for all Tauride units as well as for the Paleozoic section of the Arabian Plate. This attests for a Late Permian regional shallow marine transgression along the passive northern margin of Gondwana (Özgül, 1983). Similar to the MM,

in the Afyon zone, derived from the Taurides (Candan et al., 2005), the carpholite-bearing Triassic metaconglomerates (Pourteau, Candan, & Oberhänsli, 2010) overlie unconformably the fossiliferous Upper Permian marbles (Eldeş Formation; Özcan, Göncüoğlu, Turhan, Uysal, & Şentürk, 1988). In the Cyclades, fossiliferous Upper Permian carbonates have been documented only on two islands; Paros (Dyros unit- Anastopoulos, 1963; Papanikolaou, 1980) and Andros (Makrotantalou unit- Bulle, Bröcker, Gartner, & Keasling, 2010; Papanikolaou, 1978). In contrast to the Taurides, these Permian sections include common basic volcanic layers (Bröcker & Franz, 2006; Papanikolaou, 1980) assigned to the Permo-Triassic back-arc rifting on the active southern margin of Laurussia (Stampfli & Borel, 2004). Recently, some petrological evidence on a former high-P event (Huyskens & Bröcker, 2014) dated at 116 Ma (Cretaceous) by Ar-Ar dating of white micas (Huet, Labrousse, Monie, Malvoisin, & Jolivet, 2014) has been documented from the Makrotantalou unit. Because Cretaceous high-P metamorphism has been unknown from the CBU in the central Aegean islands, there is still a continuing debate on the Makrotantalou unit whether it belongs to Pelagonian Zone (Huet et al., 2014) or to the CBU (Gerogiannis, Xypolias, Chatzaras, Aravadinou, & Papapavlou, 2019; Huyskens & Bröcker, 2014). The Permian sections rest on both the CB and the Mesozoic series of the CBU with a tectonic contact defined as a low-angle normal fault (Huyskens & Bröcker, 2014; Bulle et al., 2010; Gautier, Brun, & Jolivet, 1993; Philippon et al., 2012; Ring, Glodny, Will, & Thomson, 2010).

Consequently, this observation leads to discuss once again the correlation of the carpholite-bearing Mesozoic section along the southern flank of the MM with the CBU based on age and high-P metamorphism. In fact, the age of high-P metamorphism defined by carpholite bearing rocks (Ar-Ar white mica age of ca. 45 Ma; Pourteau et al., 2013) coincides well with the medium-P Barrovian metamorphism (Lu - Hf garnet ages of 42.6 ± 1.9 - 34.8 ± 3.1 Ma; Schmidt, Pourteau, Candan, & Oberhänsli, 2015) obtained from the basement series of the MM. Considering the tectonostratigraphic position between two Alpine high-P units, the Lycian nappes and the Kurudere-Nebiler unit, and the tectonic model suggested for Alpine metamorphism of the MM, the differences on metamorphic grade between Kurudere-Nebiler unit and the MM can be explained by internal imbrication of the MM and burial of the Permo-Mesozoic cover series as slices to greater depths (~30 km) than the basement and Paleozoic series (~20 km) of the MM. During exhumation and southward-advancing of the Lycian nappes and overlying oceanic thrust

sheet, this high-P slice was transported to the south and placed to its current tectonostratigraphic position by Oligo-Miocene extensional uplifting of the MM.

6.2 Triassic Paleogeographical position of Cyclades/Pelagonian and MM

Numerous paleogeographical reconstruction maps have been suggested for Triassic position of the tectonic units within the Tethyan realm. In general, it is accepted that as a consequence of the opening of the southern Neotethys, a continental block including Adria, Apulia and Taurides from west to east was separated from northern margin of Gondwana during Early Triassic (Okay et al., 2006; Şengör & Yılmaz, 1981; van Hinsbergen et al., 2019) or Jurassic (Barrier, Vriekynck, Brouillet, & Brunet, 2008), while in the north of this continental block, Paleotethyan ocean was subducting northward under Laurussia (Okay, 2000; Stampfli, 2005) or southward beneath Gondwana (Göncüoğlu et al., 2000; Şengör & Yılmaz, 1981). On these maps, the relative paleogeographical positions of the Pelagonian Zone, CB, Sakarya Zone and MM that are directly related with our inferred tectonic model stand out as one of the fundamental differences. There are two views for the locations of these tectonic zones; *i*) northern margin of Gondwana (Maffione & van Hinsbergen, 2018; van Hinsbergen et al., 2019) and *ii*) southern margin of Laurussia (Stampfli, 2005; Stampfli & Hochard, 2009). In the first view, a single oceanic basin, Vardar Ocean, has been suggested and all the ophiolitic nappes in Balkan region are rooted from this ocean and transported to the south (Maffione & van Hinsbergen, 2018 and reference therein). Contrary, in the second view, a Tethyan realm consisting of multi-branches of oceanic basins and their ophiolites (i.e. Meliata, Maliac, Pindos) is assumed (Stampfli, 2005).

The Latest Neoproterozoic and Late Paleozoic (Variscan Orogeny) tectonometamorphic and magmatic evolution of these units can clarify this long-lasting debate. The CB / Pelagonian Zone and Sakarya Zone display great similarities, especially, in terms of their Late Paleozoic magmatic activity. Geochronological data reveal that the pre-Mesozoic basement of Pelagonian Zone formed at least during two distinct episodes; Neoproterozoic (U-Pb zircon ages of ca. 750-600 Ma; Zlatkin, Avigad, & Gerdes, 2017 and references therein) and Permo-Carboniferous (U-Pb zircon ages of 320 – 275 Ma; Reischmann et al., 2001; Schenker et al., 2014; Zlatkin et al., 2017 and reference therein). Late Paleozoic ages (Vavassis, de Bono, Valloton, Stampfli, & Amelin, 2000) from the high-grade hosting rocks of these intrusions (Most, 2003; Mposkos & Kostopoulos, 2001; Mposkos & Krohe, 2004) are assigned to a pre-Alpine Variscan event. The Cyclades are

regarded as the southeastern extension of the Pelagonian Zone (Anders, Reischmann, Kostopoulos, & Poller, 2006; Lamont et al., 2019). A number of granite intrusions dated at 300-315 Ma by U-Pb zircon, mid- to Late Carboniferous, clearly reveal the existence of a widespread Variscan crystalline basement (Engel & Reischmann 1998; Reischmann 1998; Tomaschek et al., 2008). Furthermore, some rare data related to a former amphibolite-facies in the country rocks of the Variscan intrusions (Andriessen, Banga, & Hebeda, 1987; Feenstra, Petrakakis, & Rhede, 2007; Franz, Okrusch, & Bröcker, 1993) are interpreted as an evidence of the Variscan metamorphism accompanying to this magmatic activity in the CB. Petrological and geochronological data obtained from Variscan granites and metamorphic rocks clearly indicate that Permo-Carboniferous age is the major continental crust-forming period in both the Pelagonian Zone and the Cyclades.

In Sakarya Zone, Carboniferous to Permian metamorphic rocks and associated magmatic arc plutons are widespread throughout the Sakarya zone of Pontides and occur as dismembered tectonic slices or autochthon basements under the Lower Jurassic to Cretaceous common cover series. The time of high-T metamorphism was dated at 330 Ma and 310 Ma by U-Pb zircon (Topuz & Altherr, 2004; Ustaömer, Robertson, Ustaömer, Gerdes, & Peytcheva, 2012a). This metamorphic basement is intruded by syn- to post-Variscan plutons dated at 330 – 310 Ma (Topuz, Candan, Okay, Albrecht, Othman, Zack, & Wang, 2019; Ustaömer, Ustaömer, & Robertson, 2012b). Variscan basement of the Sakarya Zone is placed to the active southern margin of Laurasia and its Early to Late Carboniferous metamorphic – magmatic evolution is assigned to the Variscan orogeny (Okay & Topuz, 2018).

Consequently, during Permo-Triassic, both the Pelagonian Zone / CB and Sakarya Zone are placed at the southern margin of Laurussia and are included into the Variscan Belt, extending from central Europe to the Caucasus (Neubauer, 2014; Okay & Topuz, 2018; Okay, Tüysüz, & Satır, 2006; von Raumer & Stampfli, 2008; Rolland et al., 2012; Stampfli, von Raumer, & Borel, 2002; Topuz et al., 2004).

The basement of the MM is characterized by latest Neoproterozoic to early Paleozoic poly-phase metamorphism (Candan et al., 2016; Koralay, 2015 and references therein) and accompanying voluminous granite intrusions dated at ca. 550 Ma by U-Pb zircon geochronology, which are

attributed to the final amalgamation of Gondwana (Koralay et al., 2012 and references therein). In contrast to the Pelagonian Zone and the CB, no evidence for both ca. 700 Ma and ca. 300 Ma (Variscan) deformation, metamorphism or magmatism was recognized in the MM. Considering these regional geological constrains, as a common view, it is accepted in Permo-Triassic reconstructions that the MM was part of the Anatolide-Tauride Block and constituted a part of the northern margin of Gondwana, associated to present-day Arabia (Şengör & Yılmaz, 1981; Şengör, Satır, & Akkök, 1984).

The views placing the Pelagonian Zone – CB and Sakarya Zone to the northern margin of Gondwana (Lamont et al., 2019; Maffione & van Hinsbergen, 2018; van Hinsbergen et al., 2019) in Triassic contradict with their late Carboniferous tectonometamorphic and magmatic evolution associated with the Variscan evolution of the Central Europe which is attributed to the closure of the Rheic / Rheno-Hercynian Ocean and collision of the continental block separated from Gondwana during the early Paleozoic with the Laurussia (Stampfli, von Raumer, & Borel, 2002; Okay & Topuz, 2018). Furthermore, the tectonic models (Maffione & van Hinsbergen, 2018; Lamont et al., 2019) assuming a similar paleogeographical position for Anatolides and Pelagonian / CBU to the northern margin of the Adria - Apulia – Tauride block cannot account for the E-W lateral discontinuities of the Cretaceous to early Miocene tectonic zones occurring in Greece and western Anatolia.

Consequently, these fundamental differences in Precambrian to Late Paleozoic evolution preclude to place the Pelagonian - CB – Sakarya to the same paleogeographic position (northern margin of Gondwana) with the MM. On the other hand, it was suggested by Stampfli (2005) that slab roll-back of the subducting Paleotethys triggered the opening of some oceanic branches (e.g. Pindos Ocean) along the southern margin of Laurussia and resulted in the southward drifting of these separated continental blocks (e.g. Pelagonian Zone / CB). Northward subduction of the Paleotethys led to the development of an extensional regime on the northern margin of Gondwana and resulted in the opening of the southern Neotethys (Barrier et al., 2008; Stampfli, 2005; Stampfli & Hochard, 2009). This opening was associated with separation of the Anatolide-Tauride block from Gondwana and northward drifting of this block until final collision with Laurussia during Eocene (Okay et al., 2001). As suggested in many Permo-Triassic paleogeographical reconstructions for the Tethyan realm (Blakey, 2011; Oczlon, 2006; Stampfli, 2005), this nearly synchronous drifting of the continental blocks in opposite directions from both margins of the

Paleotethys entails the existence of a transform fault system controlling these relative movements. As a result of these geological evidence, our tectonic model given below relies on the view placing the Pelagonian, CB and Sakarya to the southern margin of Laurussia in the Triassic.

6.3 Contact relationship between the CB/CBU and the MM

The contact relationship between the MM and the CBU is well exposed to the south of Tire. It has been described as a ductile thrust zone, defined by the development of a foliation in a more than 1km thick shear zone (Gessner et al., 2001; Okay, 2001 and this study). However, taking into account the striking disparities in Precambrian to Paleogene tectono-metamorphic and magmatic evolutions between the MM and the CB/CBU, it can be concluded that this contact cannot be defined as a simple thrust fault and should be related with the transform fault system discussed above.

In western Anatolia, this tectonic line may well coincide with a NE-SW- trending lithospheric strike-slip fault zone (Figure 13a), which has been suggested in many studies (e.g. Kaya, Foulger, & Şalk, 2000: Gördes Transfer Zone, Okay et al., 2012: Bornova tear fault, Ring et al., 1999, 2017: Sinistral wrench corridor, Sözbilir, İnci, Erkül, & Sümer, 2003: İzmir-Balıkesir Transfer Zone). It can provide a mechanism to explain i) the discontinuity of E-W-trending Cretaceous to Miocene metamorphic zones between Greece and western Anatolia, ii) the difference in initiation of the obduction in Greece (Late Jurassic - Early Cretaceous) and western Anatolia (Late Cretaceous), iii) the deposition of the Late Cretaceous BFZ (Okay et al., 2012), iv) distinct geochemical signatures of the Paleogene - Neogene volcanics in Rhodope and western Anatolia (Ersoy et al., 2017), differential extension between the CB/CBU and the MM during Miocene (Ring et al., 1999) and vi) active block rotations in western Anatolia (Uzel et al., 2015).

In conclusion, when combined with the regional geological constrains given above, it can be suggested that the contact between the MM and the CBU, now defined by a ductile thrust fault was originally a lithosphere-scale transform fault zone controlling the distinct Triassic to recent geodynamics on both sides of the Aegean region. However, the long-lived complex evolution of this tectonic zone needs more and precise structural studies in the Selçuk region.

6.4 Tectonic Scenario

In this section, we suggest a geodynamic model for the Late Cretaceous to Eocene subduction-related high-P metamorphism and following medium-P overprint for the CBU in western Anatolia (Figure 1 and 13). Eocene high-P metamorphism of the CB/CBU is attributed to the closure of the Pindos Ocean by northward subduction (Jolivet & Brun, 2010; Menant et al., 2016 and reference therein). Taking into account of (i) the succession of the Cycladic high-P unit consisting of polymetamorphic Variscan basement (CB) and unconformably overlaying Mesozoic passive continental margin sediments (CBU) and (ii) blueschist to eclogite facies metamorphism entailing deep burial of these continental series, the CBU should be placed at the southern margin of the Pindos Ocean. However, there is no consensus whether the Cycladic complex was an isolated continental sliver occurring in the Pindos Ocean (Ring, Johnson, Hetzel, & Gessner, 2003) or it was rifted from Laurussia and accreted to the northern margin of the Apulian platform during Late Triassic (Stampfli, 2005; Stampfli et al., 2003).

100-90 Ma (Upper Cretaceous): An Upper Cretaceous paleogeographic reconstruction including two continental blocks; i.e, Pelagonian to the north and Apulian with accreted continental sliver including Variscan basement to the south separated by the Pindos Ocean is given in Figure 13a,b. The ages of metamorphic soles from western Anatolia (Çelik, Delaloye, & Feraud, 2006; Önen, 2003; Önen & Hall, 1993; Parlak & Delaloye, 1999) and Greece (Saccani, Beccaluva, Coltorti, & Siena, 2004; Tremblay, Meshi, Deschamps, Goulet, & Goulet, 2015) mark the onset of subduction and intra-oceanic thrusting within the Neotethys during Late Cretaceous and Late Jurassic-Early Cretaceous, respectively. However, middle - late Paleocene (Ring et al., 2010) or Eocene (Jolivet & Brun, 2010) ages for the initiation of subduction is inferred for the Pindos Ocean.

~55 Ma (early Eocene): During early Eocene, the Pindos Ocean has been consumed with northward-dipping subduction giving rise to the formation of the Selçuk mélangé, which can be correlated with the Syros mélangé (Okrusch & Bröcker, 1990). (Figure 13c,d). P-T estimates (13 ± 1.5 kbar / $520 \pm 15^\circ\text{C}$) and Ar-Ar phengitic white mica ages (57.5 ± 0.3 - 54.5 ± 0.1 Ma) from the pelitic matrix of the Selçuk mélangé indicate that some slices of this accretionary complex were subducted to a depth of ca. 43 km and underwent epidote - blueschist facies metamorphism. Furthermore, P-T conditions (18 ± 2 kbar / $570 \pm 30^\circ\text{C}$) for eclogites, which were derived from the

subducted oceanic lithosphere indicate a burial depth of ca. 60 km. In eclogites, the high-P metamorphic event is dated by U-Pb zircon dating as 56.2 ± 1.5 Ma.

~45 Ma (middle Eocene): The northward subduction of the southern continental block beneath the Pelagonian microplate eventually consumed the Pindos Ocean (Figure 13e), culminating in the collision with a northern microplate (Pelagonian) in middle Eocene (Menant et al., 2016). White micas with Si content of 3.21 p.f.u. (quartz metaconglomerate) and 3.41 p.f.u. (blueschist metabasite) yielded $^{40}\text{Ar}/^{39}\text{Ar}$ ages of 44 ± 0.3 Ma (this study) and 40.1 ± 0.4 Ma (Oberhänsli et al., 1998), respectively. Similarly, U-Pb monazite dating from the coherent series (quartz metaconglomerate) yielded 40.1 ± 3.1 Ma age. P-T conditions of this series were estimated at 11.5 ± 1.5 kbar / $490 \pm 25^\circ\text{C}$. These data indicate that the coherent series in the Selçuk - Dilek area, which was derived from the southern continental block, was buried to a depth of ca. 38 km and was subjected to epidote - blueschist facies metamorphism during the early Eocene (Figure 13e).

45-34 Ma (middle – late Eocene): Low-Si (3.04 p.f.u.) white micas from retrogressed blueschist metapelites of the coherent series were dated at ca. 36 – 34 Ma by $^{40}\text{Ar}/^{39}\text{Ar}$ method (this study), latest Eocene. Similarly, U-Pb dating of syntectonic allanite from the retrograded matrix of the Selçuk mélange yielded an age of 31.6 ± 6.6 Ma. Furthermore, the Ar-Ar white mica age at ca. 37 Ma from Samos has been obtained from the Ampelos nappe (Ring & Layer, 2003). Based on this radiometric data and P-T estimations, the time of tectonically juxtaposition of coherent series and Selçuk mélange can be considered as latest Eocene. Considering the estimated pressure of 6-7 kbar for the retrograde overprint under greenschist facies conditions for the two units, a depth of 15-20 km for this tectonic juxtaposition can be proposed. Taking into account of the petrological evidence from the eclogites in the Selçuk mélange indicating retrogression under Barrovian-type medium-P conditions ($505 \pm 25^\circ\text{C}$ / 6 ± 1 kbar) without any blueschist overprint during exhumation, it can be assumed that the eclogites were incorporated into the mélange at this stage. Furthermore, 35.1 ± 0.3 Ma $^{40}\text{Ar}/^{39}\text{Ar}$ age of low-Si white mica from the shear zone separating the MM from the CBU can be interpreted as the time of tectonic juxtaposition of these two crystalline complexes under greenschist facies conditions during latest Eocene.

7. CONCLUSIONS

Eclogite and blueschist facies rocks cropping out in western Anatolia form the eastward continuation of the CBU in Turkey. It occurs a tectonic unit between the underlying MM and the overlying Afyon Zone / Lycian Nappes and the BFZ. This HP unit is attributed to the closure of the Pindos Ocean and is made up of two tectonic units which were tectonically juxtaposed under greenschist facies conditions; (i) coherent series represented by Triassic to Upper Cretaceous passive continental margin sediments and (ii) Upper Cretaceous Selçuk mélange consisting of pelitic blueschist matrix with eclogite blocks. The pelitic matrix of the Selçuk mélange yields Ar-Ar white mica ages of 57.5 ± 0.3 and 54.5 ± 0.1 Ma interpreted as the age of epidote-blueschist facies metamorphism ($520 \pm 15^\circ\text{C}$ / 13 ± 1.5 kbar). Eclogite facies metamorphism ($570 \pm 30^\circ\text{C}$ / 18 ± 2 kbar) in the eclogite blocks was dated at 56.2 ± 1.5 Ma by U-Pb zircon method, early Eocene. The pelitic matrix of the mélange lacks petrological and textural evidence indicating a former eclogite facies metamorphism. This observation raises the questions whether this is a result of high degree retrogression of the pelitic matrix of the mélange while the eclogites were preserved or the matrix of the mélange has never experienced an eclogite facies metamorphism. Considering the lack of blueschist overprint in the eclogites, it can be interpreted that eclogites were subjected to isothermal decompression during exhumation and were incorporated into the Selçuk mélange under medium-P conditions ($\sim 6\text{-}7$ kbar / $490 \pm 40^\circ\text{C}$). The coherent series has experienced epidote - blueschist facies metamorphism (11.5 ± 1.5 kbar / $490 \pm 25^\circ\text{C}$) corresponding to a burial depth of 38 km during middle Eocene, Ar-Ar white mica and U-Pb monazite ages of ca. 44 - 40 Ma . The retrograde overprint of coherent series ($410 \pm 15^\circ\text{C}$ / 7 ± 1.5 kbar from Dilek Peninsula; $485 \pm 33^\circ\text{C}$ / $\sim 6\text{-}7$ kbar from Selçuk – Tire area) and Selçuk mélange ($510 \pm 15^\circ\text{C}$ / 6 ± 1 kbar) was dated at 36-34 by Ar-Ar white mica and U-Pb monazite and 31 Ma by U-Pb allanite dating, respectively. Considering the regional geological constrains Triassic to recent, it can be envisaged that the contact between MM and CBU, now defined by a ductile thrust fault, originally was a lithosphere-scale transform fault zone. Based on Ar-Ar white mica ages from this contact, the time of tectonic juxtaposition of the CBU and the MM under greenschist facies conditions occurred at 35.1 ± 0.3 Ma, during late Eocene.

ACKNOWLEDGEMENTS

This cooperation was and is substantially supported by the Volkswagen Stiftung, the German Science Foundation DFG (grant OB 80/22), TÜBİTAK (grant YDABÇAG-494), Dokuz Eylül

University BAP grant (0.922.98.01.06) and the German academic exchange organization DAAD. The support of all these granting agencies is warmly acknowledged. Thanks are due to Christina Günter (Potsdam University) for assistance with microprobe. Bénédicte Cenki-Tok thanks O. Bruguier for assistance during LA-ICPMS analysis. Bénédicte Cenki-Tok acknowledges funding from the European Union's Horizon 2020 research and innovation programme under grant agreement No 793978.

Accepted Article

REFERENCES

- Alan, İ., Keskin, H., Altın, İ., Böke, N., Balcı, V., Elibol, H., ... Candan, O. (2019). Batı Anadolunun tektonostratigrafik özellikleri. MTA bilimsel etkinlikler haftası 11-15 şubat 2019, Ankara, Bildiri özleri, 25-66.
- Anastopoulos, J. (1963). Geological study of Antiparos island group. *Geology Geophysics Reservoir*, IGMR, 7: 231-375. Athens.
- Anders, B., Reischmann, T., Kostopoulos, D., & Poller, U. (2006). The oldest rocks of Greece: first evidence for a Precambrian terrane within the Pelagonian Zone. *Geological Magazine*, 143, 41–58.
- Barrier, E., Vriekynck, B., Bergerat, F., Brunet, M.F., Mosar, J., Poisson, A., & Sosson, M. (2008). Palaeotectonic maps of the Middle East: tectono-sedimentary-palinspastic maps from Late Norian to Pliocene. Commission for the Geological map of the World (CGMW/CCGM)/UNESCO. (<http://www.ccgm.org>) Atlas of 14 maps. Scale 1/18500000.
- Barrier, E., Vriekynck, B., Brouillet, J.F., Brunet, M.F. (2008). Paleotectonic reconstruction of the central Tethyan realm. (CGMW/CCGM), (<http://www.ccgm.org>) Atlas of 20 maps, Darius Programme.
- Başarır, E., & Konuk, Y. T. (1981). Gümüldür yöresinin kristalin temeli ve allohton birimleri. *Türkiye Jeoloji Kurumu Bülteni*, 2 (24), 1-6, Ankara.
- Bhattacharya, A., Mohanty, L., Maji, A., & Sen, S.K. (1992). Non-ideal mixing in the phlogopite-alline binary: contrasts from experimental data on Mg-Fe partitioning and a formulation of the biotite-garnet geothermometry. *Contribution to Mineralogy and Petrology*, 111, 87-93.
- Blakey, R. (2011). Paleogeographic maps. European paleogeography. Triassic (225 Ma). <http://cpgeosystems.com>.
- Bonneau M. (1984). Correlation of the Hellenide nappes in the southeast Aegean and their tectonic reconstruction. *Geological Society of London Special Publication*. 17, 517–27.
- Bosch, D., Garrido, C.J., Bruguier, O., Dhuime, B., Bodinier, J.L., Padron-Navarta, J.A., & Galland, B. (2011). Building an island-arc crustal section: time constraints from a LA-ICP-MS zircon study. *Earth and Planetary Science Letters*, 309, 268–279.

Bröcker, M., & Franz, L. (2006). Dating metamorphism and tectonic juxtaposition on Andros Island (Cyclades, Greece): results of a Rb–Sr study. *Geological Magazine*, 143(5), 609-620.

Bröcker, M., Löwen, K., & Rodinov, N. (2014) Unraveling protolith ages of meta-gabbros from Samos and the Attic–Cycladic Crystalline Belt, Greece: Results of a U–Pb zircon and Sr–Nd whole rock study. *Lithos*, 198-199, 234-248.

Bröcker, M., Kreuzer, H., Matthews, A., & Okrusch, M. (1993). $^{40}\text{Ar}/^{39}\text{Ar}$ and oxygen isotope studies of polymetamorphism from Tinos Island, Cycladic blueschist belt. *Journal of Metamorphic Geology*, 11, 223–240.

Bulle, F., Bröcker, M., Gartner, C., & Keasling, A. (2010). Geochemistry and geochronology of HP mélanges from Tinos and Andros, Cycladic blueschist belt, Greece. *Lithos*, 117, 61-81.

Bruguier, O., Hammor, D., Bosch, D., & Caby, R. (2009). Miocene incorporation of peridotite into the Hercynian basement of the Maghrebides (Edough Massif, NE Algeria): implications for the geodynamic evolution of the Western Mediterranean. *Chemical Geology*, 261, 171–183

Candan, O., Akal, C., Koralay, O.E., Okay, A.I., Oberhänsli, R., Prelevic, D., ... Mertz-Kraus, R. (2016). Carboniferous Granites on the Northern Margin of Gondwana, Anatolide-Tauride Block, Turkey—Evidence for Southward Subduction of Paleotethys. *Tectonophysics*, 683, 349-366.

Candan, O., Çetinkaplan, M., Oberhänsli, R., Rimmele, G., & Akal, C. (2005). Alpine high pressure/low temperature metamorphism of Afyon Zone and implication for metamorphic evolution of western Anatolia, Turkey. *Lithos*, 84, 102–124.

Candan, O., Dora, O.Ö., Oberhänsli, R., Oelsner, F., & Dürr, S. (1997). Blueschist relicts in the Mesozoic cover series of the Menderes Massif and correlations with Samos Island, Cyclades. *Schweizerische Mineralogische und Petrographische Mitteilungen*, 77, 95-99.

Candan O, R., Dora, Ö., Çetinkaplan, M., Koralay, E., Rimmele, Gaetan., ... Akal C. (2011a). Polymetamorphic evolution of the Pan-African Basement and Paleozoic – Early Tertiary cover series of the Menderes Massif. *Bulletin of the Mineral Research and exploration*, 142, 121-165.

Candan, O., Koralay, O.E., Akal, C., Kaya, O., Oberhänsli, R., Dora, O.Ö., ... Chen, F. (2011b). Supra-Pan-African unconformity between core and cover series of the Menderes Massif / Turkey and its geological implications. *Precambrian Research*, 184, 1–23.

Cenki-Tok, B., Expert, M., Işık, V., Candan, O., Monie, P., & Bruguier, O. (2015). Complete Alpine reworking of the northern Menderes Massif, western Turkey. *International Journal of Earth Science*, 105(5), 1507-1524.

Çelik, Ö.F., Delaloye, M. & Feraud, G. (2006). Precise Ar-Ar ages from metamorphic sole rocks of the Tauride belt ophiolites, southern Turkey: implications for the rapid cooling history. *Geological Magazine*, 143, 213-227.

Darling, J.R., Storey, C.D., & Engi, M. (2012). Allanite U–Th–Pb geochronology by laser ablation ICPMS. *Chemical Geology*, 292–293:103–115.

De Capitani, C. (1994). Gleichgewichts-phaseendiagramme: Theorie und Software. *Berichte der Deutschen Mineralogischen Gesellschaft*, 6, 48.

De Capitani, C., & Petrakakis, K. (2010). The computation of equilibrium assemblage diagrams with Theriak/Domino software. *American Mineralogist*, 95, 1006–1016.

Ellis, D.J., & Green, D.H. (1979). An experimental study of the effect of Ca upon garnet–clinopyroxene Fe–Mg exchange equilibria. *Contributions to Mineralogy & Petrology*, 71, 13–22

Engel, M., & Reischmann, T. (1998). Single zircon geochronology of orthogneisses from Paros, Greece. *Bulletin of Geological Society of Greece*, 32(3), 91–99.

Ersoy, E.Y., Akal, C., Genç, Ş.C., Candan, O., Palmer, M.R., Prelevic, D., ... Mertz-Kraus, R. (2017) U-Pb zircon geochronology of the Paleogene – Neogene volcanism in the NW Anatolia: Its implications for the Late Mesozoic-Cenozoic geodynamic evolution of the Aegean. *Tectonophysics*, 717, 284-301.

Faulp, A., Pavlopoulos, A., Klötzli, U., & Petrakakis, K. (2006). On the provenance of mid-Cretaceous turbidites of the Pindos zone (Greece): implications from heavy mineral distribution, detrital zircon ages and chrome spinel chemistry. *Geological Magazine*, 143 (3), pp. 329-342

Feenstra, A., Petrakakis, K., & Rhede, D. (2007) Variscan relicts in Alpine high-P pelitic rocks from Samos (Greece): evidence from multi-stage garnet and its included minerals. *Journal of Metamorphic Geology*, 25, 1011-1033.

Flansburg, M.E., Stockli, D.F., Poulaki, E., & Soukis, K. (2019) Tectono-Magmatic and Stratigraphic Evolution of the Cycladic Basement, Ios Island, Greece. *Tectonics*, DOI: 10.1029/2018TC005436.

Fleck, R. J., Sutter, J. F., & Elliot, D. H. (1977). Interpretation of discordant $^{40}\text{Ar}/^{39}\text{Ar}$ age-spectra of Mesozoic tholeiites from Antarctica. *Geochimica Cosmochimica Acta*, 41, 15-32.

Forster, M. A., & Lister, G. S. (2005). Several distinct tectonometamorphic slices in the Cycladic eclogite-blueschist belt, Greece. *Contributions to Mineralogy & Petrology*, 150, 523–545.

Franz, L., Okrusch, M., & Bröcker, M. (1993). Polymetamorphic evolution of pre-Alpine basement rocks on the island of Sikinos (Cyclades, Greece). *Neues Jahrbuch Mineralogie Monatshefte*, Jg, 1993, 145–162.

Gerogiannis, N., Xypolias, P., Chatzaras, V., Aravadinou, E., & Papapavlou, K. (2019). Deformation within the Cycladic subduction–exhumation channel: new insights from the enigmatic Makrotantalo nappe (Andros, Aegean), *International Journal of Earth Science*, 108(3), 817-843.

Gessner, K., Ring, U., Johnson, C., Hetzel, R., Passchier, C.W., & Güngör, T. (2001). An active bivergent rolling-hinge detachment system: the Central Menderes metamorphic core complex in western Turkey. *Geology*, 29, 611-614.

Göncüoğlu, M.C., Turhan, N., Şentürk, K., Özcan, A., Uysal, Ş., & Yalınız, M.K. (2000). A geotraverse across northwestern Turkey: tectonic units of the Central Sakarya region and their tectonic evolution. *Geological Society Special Publication* 173, 139-161.

Graham, C.M., & Powell, R. (1984). A garnet-hornblende geothermometer: calibration testing and application to the Pelona schist, Southern California. *Journal of Metamorphic Geology*, 2, 13–31.

Green, D.H., & Hellman, P.L. (1982). Fe–Mg partitioning between coexisting garnet and phengite at high pressure, and comments on a garnet–phengite geothermometer. *Lithos*, 15, 253–266.

Gunther, D., & Heinrich, C.A. (1999). Enhanced sensitivity in LA-ICPMS using helium–argon mixture as aerosol carrier. *Journal of Analytical Atomic Spectrometry*, 14, 1369–1374.

Halama, R., Konrad-Schmolke, M., Sudo, M., Marschall, H., & Wiedenbeck, M. (2014). Effects of fluid–rock interaction on $^{40}\text{Ar}/^{39}\text{Ar}$ geochronology in high-pressure rocks (Sesia-Lanzo Zone, Western Alps). *Geochimica et Cosmochimica Acta*, 126, 475-494.

- Hodges, K.V., & Crowley, P.D. (1985). Error estimation and empirical geothermobarometry for pelitic systems. *American Mineralogist*, 70, 702-709.
- Hodges, K., & Spear, F. S. (1982). Geothermometry, geobarometry and the Al_2SiO_5 triple point at Mt. Moosilauke, New Hampshire. *American Mineralogist*, 67(11-12), 1118-1134.
- Holland, T.J.B. (1980). The reaction albite=jadeite+quartz determined experimentally in the range 600-1200 °C. *American Mineralogist*, 65, 129-134.
- Holland, T., & Blundy, J. (1994). Non-ideal interactions in calcic amphiboles and their bearing on amphibole-plagioclase thermometry. *Contributions to Mineralogy & Petrology*, 116, 433-447.
- Holland, T.J.B., & Powell, R. (1998). An internally-consistent thermodynamic dataset for phases of petrological interest. *Journal of Metamorphic Geology*, 16, 309–344.
- Huet, B., Labrousse, L., Monie, P., Malvoisin, B., & Jolivet, L. (2015). Coupled phengite $^{40}\text{Ar}/^{39}\text{Ar}$ geochronology and thermobarometry: P-T-t evolution of Andros Island (Cyclades, Greece). *Geological Magazine*, 152, 711–727.
- Huyskens, M. H. & Bröcker, M. 2014. The status of the Makrotantalou Unit (Andros, Greece) within the structural framework of the Attic-Cycladic Crystalline Belt. *Geological Magazine*, 151(3), 430–46.
- Ishizuka, O. (1998). Vertical and horizontal variation of the fast neutron flux in a single irradiation capsule and their significance in the laser-heating $^{40}\text{Ar}/^{39}\text{Ar}$ analysis: Case study for the hydraulic rabbit facility of the JMTR reactor, Japan. *Geochemical Journal*, 32, 243-252.
- Jackson, S.E., Perason, N.J., Griffin, W.L., & Belousova, E.A. (2004). The application of laser ablation inductively coupled plasma-mass spectrometry to in situ U-Pb zircon geochronology. *Chemical Geology*, 21, 47-69.
- Jacobshagen, V. (1986). *Geologie von Griechenland*. Berlin, Stuttgart. Gebruder Borntraeger, 363 pp.
- Jaffey, A.H., Flynn, K. F., Glendenin, L. E., Bentley, W.C., & Essling, A.M. (1971). Precision measurement of the half-lives and specific activities of ^{235}U and ^{238}U . *Physical Review*, C4, 1889-1907.

Jolivet, L., & Brun, J.P. (2010). Cenozoic geodynamic evolution of the Aegean region. *International Journal of Earth Science*, 99, 109–138.

Jolivet, L., Faccenna, C., Huet, B., Labrousse, L., Le Pourhiet, L., Lacombe, O., ... Driussi, O. (2013). Aegean tectonics: strain localization, slab tearing and trench retreat. *Tectonophysics*, v. 597-598, 1-33.

Jolivet, L., Lecomte, E., Huet, B., Denèle, Y., Lacombe, O., Labrousse, L., ... Mehl, C. (2010). The North Cycladic Detachment System. *Earth Planetary Science Letters*, 289, 87–104.

Jolivet, L., Rimmelé, G., Oberhänsli, R., Goffé, B., & Candan, O. (2004). Correlation of syn-orogenic tectonic and metamorphic events in the Cyclades, the Lycian Nappes and the Menderes massif, geodynamic implications. *Bulletin of Society Geology France*, 175, 217–238.

Kaya, O., Foulger, G.R., & Şalk, M. (2000). The Gördes Fault zone of central western Anatolia: The Pliocene to Recent passive transfer zone. *International Earth Science Colloquium on the Aegean Region, IESCA-2000*, 35 s.

Kohn, M.J., & Spear, F.S. (1989). Empirical calibration of geobarometers for the assemblage garnet + hornblende + plagioclase + quartz. *American Mineralogist*, 74, 77-84.

Koralay, O.E. (2015). Late Neoproterozoic granulite facies metamorphism in the Menderes Massif, Western Anatolia/Turkey: Implication for the assembly of Gondwana. *Geodinamica Acta*, 27 (4), 244-266

Koralay, O.E., Candan, O., Chen, F., Akal, C., Oberhänsli, R., Satır, M., & Dora, O.Ö. (2012). Pan-African magmatism in the Menderes Massif: geochronological data from leucocratic tourmaline orthogneisses in western Turkey. *International Journal of Earth Sciences*, 101, 2055–2081.

Krogh, E.J. (1988). The garnet–clinopyroxene Fe–Mg geothermometer a re-interpretation of existing experimental data. *Contributions to Mineralogy & Petrology*, 99, 44–48.

Lamont, T.N., Roberts, N.M., Searle, M.P., Gopon, P., Waters, D., & Miller, I. (2019). The age, origin and emplacement of the Tsiknias Ophiolite, Tinos, Greece. *American Geophysical Union*,

doi: 10.1029/2019TC005677.

Leake, B.A., Woolley, A.R., Arps, C.E.S., Birch, W.D., Gilbert, M.C., Grice, J.D., ... Youzmi, G. (1997). Nomenclature of amphiboles. Report of the Subcommittee on Amphiboles of the International Mineralogical Association Commission on New Minerals and Mineral Names. *European Journal of Mineralogy*, 9, 623–651.

Ludwig, K.R. (2001). ISOPLOT/Ex, version 2.49: A geochronological toolkit for Microsoft Excel. Berkeley Geochronology Center, Special Publication 1a, 1-56.

Maffione, M., & van Hinsbergen, D. J. J. (2018). Reconstructing plate boundaries in the Jurassic Neo-Tethys from the East and West Vardar Ophiolites (Greece and Serbia). *Tectonics*, v. 37, pp. 858–887.

McDougall, I., & Harrison, T. M. (1999). Geochronology and thermochronology by the $^{40}\text{Ar}/^{39}\text{Ar}$ method. Oxford University Press, New York, 269 pp.

Menant, A., Jolivet, L., & Vrielynck, B. (2016). Kinematic reconstructions and magmatic evolution illuminating crustal and mantle dynamics of the eastern Mediterranean region since the Late Cretaceous. *Tectonophysics*, 675, 103–140.

Molina, J.F., Moreno, J.A., Catro, A., Rodriguez, C., & Fershtater, G.B. (2015). Calcic amphibole thermobarometry in metamorphic and igneous rocks: New calibrations based on plagioclase/amphibole Al-Si partitioning and amphibole/liquid Mg partitioning. *Lithos*, 232, 286-305.

Morimoto, N., Fabries, J., Ferguson, A.K., Ginzburg, I.V., Ross, M., ... Zussman, J.Z. (1988), Nomenclature of pyroxenes. *American Mineralogist*, 73, 1123–1133.

Most, T. (2003). Geodynamic Evolution of the Eastern Pelagonian Zone in North western Greece and the Republic of Macedonia. Implications From U/Pb, Rb/Sr, K/Ar, $^{40}\text{Ar}/^{39}\text{Ar}$ Geochronology and Fission Track Thermo chronology. Unpublished PhD. Thesis, Universität Tübingen, Germany (98pp).

Mposkos, E., & Krohe, A. (2004). New evidences of the low-P / high-T pre-Alpine metamorphism and medium-P Alpine overprint of the Pelagonian zone documented in metapelites and orthogneisses from the Voras Massif, Macedonia, northern Greece. *Bulletin Geology of Society Greece*, 26, 558–567.

Neubauer, F. (2014). Gondwanaland goes Europe. *Australian Journal of Earth Science*, 107 (1), 147–155.

Oberhänsli, R., Monie, P., Candan, O., Warkus, F., Partzsch, J.H., & Dora, O.Ö. (1998). The age of blueschist metamorphism in the Mesozoic cover series of the Menderes Massif. *Schweizerische Mineralogische und Petrographische Mitteilungen*, 78, 309-316.

Oczlon, M.S. (2006). *Terrane map of Europe*, 1st edition, Gaea Heidelbergensis, v.15.

Okay, A.I. (2000). Was the Late Triassic orogeny in Turkey caused by the collision of an oceanic plateau? *Geological Society Special Publication* 173, 25-41.

Okay, A.I. (2001). Stratigraphic and metamorphic inversions in the central Menderes Massif: a new structural model. *International Journal of Earth Science*, 89, 709-727.

Okay, A.I., & Topuz, G. (2018). Variscan orogeny in the Black Sea region. *International Journal of Earth Sciences*, 106, 569–592.

Okay, A.I., İrintek, İ., Altın, D., Özkan-Altın, S., & Okay, N. (2012). An olistostrome-mélange belt formed along a major suture: Bornova Flysch Zone, western Turkey. *Tectonophysics*, 568-569, 282-295.

Okay, A., Tansel, I., & Tüysüz, O. (2001). Obduction, subduction and collision as reflected in the Upper Cretaceous – Lower Eocene sedimentary record of western Turkey. *Geological Magazine*, 138(2), 117-142.

Okay, A. I., & Tüysüz, O. (1999). Tethyan sutures of northern Turkey. In: Durand, B., Jolivet, L., Horvath, F., & Serrano, M. (eds). *The Mediterranean Basin: Tertiary Extension within the Alpine Orogeny*. Geological Society of London, Special Publications, 156, 475-515.

Okay, A.I., Tüysüz, O., & Satır, M. (2006). Cretaceous and Triassic subduction-accretion, HP/LT metamorphism and continental growth in the Central Pontides, Turkey. *Geological Society of America Bulletin*, 118, 1247–69.

Okrusch, M., & Bröcker, M. (1990). Eclogites associated with high-grade blueschist in the Cyclades archipelago. Greece. *A review European Journal of Mineralogy*, 2, 451-478.

Önen, P. (2003). Neotethyan ophiolitic rocks of the Anatolides of NW Turkey and comparison with Tauride ophiolites. *Journal of Geological Society London*, 160, 947-962.

Özcan, A., Göncüoğlu, M.C., Turhan, N., Uysal, S., & Şentürk, K. (1988). Late Paleozoic evolution of the Kütahya – Bolcardağ belt, *METU Journal of Pure and Applied Sciences*, 21, 211-220.

Özer, S. (1993). Upper Cretaceous rudists from the Menderes Massif. 6th Congress of the Geological Soc. of Greece. Bulletin Geological Society of Greece, 28(3):55–73.

Özer, S., Sözbilir, H., Özkar, I., Toker, V., & Sarı, B. (2001). Stratigraphy of Upper Cretaceous–Paleogene sequences in the southern and eastern Menderes Massif (Western Turkey). International Journal of Earth Science, 89, 852– 866.

Özgül, N. (1983). Stratigraphy and tectonic evolution of the central Taurides. International symposium, Geology of the Taurus belt, 26-29 September Ankara, 77-90.

Papanikolaou, D. (1978). Contribution to the geology of the Aegean Sea; the island of Andros. Annales Geologiques des Pays Helleniques, 29(2), 477–553.

Papanikolaou, D. (1980). Contribution to the geology of Aegean Sea. The Island of Paros. Annales Geologiques des Pays Helleniques, 30, 65-96.

Papanikolaou, D.J. (1984). The three metamorphic belts of the Hellenides: a review and a kinematic interpretation. Geological Society of London, Special Publications, 17(1), 551–561.

Papanikolaou, D. (2009). Timing of tectonic emplacement of the ophiolites and terrane paleogeography in the Hellenides. Lithos, 108, 262–280.

Papanikolaou, D. (2013). Tectonostratigraphic models of the Alpine terranes and subduction history of the Hellenides. Tectonophysics, 595–596, 1–24.

Parlak, O., & Delaloye, M. (1999). Precise $^{40}\text{Ar}/^{39}\text{Ar}$ ages from the metamorphic sole of the Mersin ophiolite (Southern Turkey). Tectonophysics, 301, 145-158.

Philippon, M., Brun, J.P., & Gueydan, F. (2012). Deciphering subduction from exhumation in the segmented Cycladic Blueschist Unit (Central Aegean, Greece). Tectonophysics, 524–525, 116–134.

Poitrasson, F., Chenery, S., & Shepperd, T.J. (2000). Electron microprobe and LA-ICP-MS study of monazite hydrothermal alteration: implications for U–Th–Pb geochronology and nuclear ceramics. Geochimica et Cosmochimica Acta, 64, 3283–3297.

Pourteau, A., Candan, O., & Oberhänsli, R. (2010). High-pressure metasediments in central Turkey: constraints on the Neotethyan closure history. Tectonics, 29. doi: 10. 1029 /2009TC002650

Pourteau, A., Oberhänsli, R., Candan, O., Barrier, E., & Vrielynck, B. (2016). Neotethyan closure history of western Anatolia: a geodynamic discussion. *International Journal of Earth Sciences*, 105(1), 203-224.

Pourteau, A., Sudo, O., Candan, O., Lanari, P., Vidal, O., & Oberhänsli, R. (2013). Neotethys closure history of Anatolia: insights from ^{40}Ar – ^{39}Ar geochronology and P–T estimation in high-pressure metasedimentary rocks. *Journal of Metamorphic Geology*, doi:10.1111/jmg.12034

Reischmann, T. (1998). Pre-alpine origin of tectonic units from the metamorphic complex of Naxos, Greece, identified by single zircon Pb/Pb dating. *Bulletin Geological Society Greece*, 32(3), 101–111.

Reischmann, T., Kostopoulos, D.K., Loos, S., Anders, B., Avgerinas, A., & Sklavounos, S.A. (2001). Late Paleozoic magmatism in the basement rocks South West of the Mt. Olympos, Central Pelagonian Zone, Greece: remnants of a Permo-Carboniferous magmatic arc. *Bulletin Geological Society Greece*, 25, 985–993.

Rimmele, G., Jolivet, L., Oberhänsli, R. & Goffé, B. (2003). Deformation history of the high-pressure Lycian Nappes and implications for tectonic evolution of SW Turkey. *Tectonics*, 22(2), 1007.

Rimmelé, G., Oberhänsli, R., Candan, O., Goffé, B., & Jolivet, L. (2006). The wide distribution of HP–LT rocks in the Lycian Belt (Western Turkey). Implications for the accretionary wedge geometry. *Journal of Geological Society London Special Publications*, 260, 447–466.

Ring, U., Gessner, K., & Thomson, S. (2017) Variations in fault-slip data and cooling history reveal corridor of heterogeneous back-arc extension in the eastern Aegean Sea region. *Tectonophysics*, doi: 10.1016/j.tecto.2017.02.013

Ring, U., Glodny, J., Will, T., & Thomson, S. (2010). The Hellenic subduction system: high pressure metamorphism, exhumation, normal faulting, and large-scale extension. *Annual Review Earth Planetary Science*, 38 (1), 45–76.

Ring, U., Johnson, C., Hetzel, R., & Gessner, K. (2003). Tectonic denudation of a Late Cretaceous – Tertiary collisional belt: Regionally symmetric cooling patterns and their relation to extensional faults in the Anatolide belt of western Turkey. *Geological Magazine*, 140, 421 – 441.

Ring, U., Lams, S., & Bernet, M. (1999). Structural analysis of a complex nappe sequence and late-orogenic basins from the Aegean Samos Island, Greece. *Journal of Structural Geology*, 21, 1575- 1601,

Ring, U., & Layer, P.W. (2003). High-pressure metamorphism in the Aegean, eastern Mediterranean: underplating and exhumation from the late Cretaceous until the Miocene to Recent above the retreating Hellenic subduction zone. *Tectonics*, 22(3), doi:10.1029/2001TC001350.

Ring, U., Will, T., Glodny, J., Kumerics, C., & Gessner K. (2007). Early exhumation of high-pressure rocks in extrusion wedges: Cycladic blueschist unit in the eastern Aegean, Greece, and Turkey. *Tectonics*, 26, TC2001.

Roche, V., Conand, C., Jolivet, L., & Augier, R., (2018). Tectonic evolution of Leros Island (Dodecanese, Greece) and correlation between Aegean domain and Menderes Massif. *Journal of Geological Society*, doi.org/10.1144/jgs2018-028.

Rolland, Y., Perinçek, D., Kaymakçı, N., Sosson M., Barrier, E., & Avagyane, A. (2012). Evidence for 80–75 Ma subduction jump during Anatolide–Tauride–Armenian block accretion and 48 Ma Arabia-Eurasia collision in Lesser Caucasus–East Anatolia. *Journal of Geodynamic*, 56–57, 76–85.

Saccani, E., Beccaluva, L., Coltorti, M., & Siena, F. (2004). Petrogenesis and tectono-magmatic significance of the Albanide – Hellenide suppelagionian ophiolites. *Ofioliti*, 29(1), 75-93.

Schenker, F.L., Burg, J.-P., Kostopoulos, D., Moulas, E., Larionov, A., & von Quadt, A. (2014). From Mesoproterozoic magmatism to collisional Cretaceous anatexis: tectono-magmatic history of the Pelagonian Zone, Greece. *Tectonics*, 33,1552–1576.

Schmädicke, E., & Will, T.M. (2003). Pressure-temperature evolution of blueschist facies rocks from Sifnos, Greece, and implications for the exhumation of high-pressure rocks in the central Aegean. *Journal of Metamorphic Geology*, 21,799–81.

Schmidt, M.W., & Poli, S. (1994). The stability of lawsonite and zoisite at high pressures: Experiments in CASH to 92 kbar and implications for the presence of hydrous phases in subducted lithosphere. *Earth and Planetary Science Letters*, 124, 105-118.

Schmidt, A., Pourteau, A., Candan, O., & Oberhänsli, O. (2015). Lu–Hf geochronology on cm-sized garnets using microsampling: New constraints on garnet growth rates and duration of metamorphism during continental collision (Menderes Massif, Turkey). *Earth and Planetary Science letters*, 432, 24-35.

Sözbilir, H., Inci, U., Erkül, F., & Sümer, Ö. (2003). An active intermittent transfer zone accommodating N–S extension in western Anatolia and its relation to the North Anatolian fault system. In: *International Workshop on the North Anatolian, East Anatolian and Dead Sea Fault Systems. Recent Progress in Tectonics and Palaeo-seismology and Field Training Course in Palaeoseismology*, Ankara, Abstracts, p.87.

Stacey, J.S., & Kramers, D.J. (1975). Approximation of terrestrial lead isotope evolution by a 2-stage model. *Earth Planetary Science letters*, 26(2), 207-221.

Stampfli, G.M. (2005). Plate tectonic of the Apulia-Adria microcontinents. In: Finetti, I. R. (ed.) *Crop Project deep seismic exploration of the Mediterranean and Italy*. Elsevier, The Netherlands, 747–766.

Stampfli, G. M., & Borel, G.D. (2004). The transmed transects in space and time: constraints on the paleotectonic evolution of the mediterranean domain. in: Cavazza, W., Roure, F., Spakman, W., Stampfli, G.M., & Ziegler, P. (eds) *The transmed atlas: the mediterranean region from crust to mantle*. Springer verlag, Germany, 53–80.

Stampfli, G.M., & Hochard, C. (2009). Plate tectonics of the Alpine realm. In: Murphy, J.B., Hynes, A.J., Keppie, J.D. (Eds.), *Ancient orogens and modern analogues*. Geological Society, London, Special Publications, 327, pp. 89–111.

Stampfli, M.G., von Raumer, J.F., & Borel, G.D. (2002). Paleozoic evolution of Pre-Variscan terranes: From Gondwana to the Variscan collision. *Geological Society of America Special Paper* 364, 263-280.

Stampfli, G.M., Vavassis, I., De Bono, A., Rosselet, F., Matti, B., & Bellini, M. (2003). Remnants of the Paleotethys oceanic suture-zone in the western Tethyan area. In: Cassinis, G., Decandia, F.A. (Eds.), *Stratigraphic and Structural Evolution on the Late Carboniferous to Triassic Continental and Marine Successions in Tuscany (Italy)*. *Regional Reports and General Correlation: Bolletino della Società Geologica Italiana, Volume speciale 2*, pp. 1–24.

Steiger, R.H., & Jager, E. (1977). Subcommisison on geochronology: Convention on the use decay constants in geo- and cosmochronology. *Earth Planetary Science Letters*, 36, 359-362.

Şengör, A.M.C., Satır, M., & Akkök, R. (1984). Timing of tectonic events in the Menderes Massif, western Turkey: implication for tectonic evolution and evidence for Pan-African basement in Turkey. *Tectonics*, 3, 693-707.

Şengör, A.M.C., & Yılmaz, Y. (1981). Tethyan evolution of Turkey: a plate tectonic approach. *Tectonophysics*, 75,181-241.

Tera, F., & Wasserburg, G. (1972). U–Th–Pb systematics in three Apollo 14 basalts and the problem of initial Pb in lunar rocks. *Earth Planetary Science Letters*, 14, 281–304.

Tomaschek, F., Keiter, M., A. Kennedy., & Ballhaus, C. (2008). Pre-Alpine basement within the Northern Cycladic Blueschist Unit on Syros Island, Greece. *Zeitschrift der Deutschen Gesellschaft für Geowissenschaften*, 159(3), 521–532.

Tomaschek, F., Kennedy, A., Villa, I., Lagos, M., & Ballhaus, C. (2003). Zircons from Syros, Cyclades, Greece-Recrystallization and mobilization during high pressure metamorphism. *Journal of Petrology*, 44, 1977 – 2002.

Topuz, G., & Altherr, R. (2004). Pervasive rehydration of granulites during exhumation-an example from the Pular complex, Eastern Pontides, Turkey. *Mineralogy and Petrology*, 81, 165–185.

Topuz, G., Altherr, R., Kalt, A., Satır, M., Werner, O., & Schwartz, W.H. (2004). Aluminous granulites from the Pular Complex, NE Turkey: a case of partial melting, efficient melt-extraction and crystallization. *Lithos*, 72, 183–207.

Topuz, G., Candan, O., Okay, A.I., von Quadt, A., Othman, M., Zack, T., & Wang, J. (2019). Silurian anorogenic basic and acidic magmatism in northwest Turkey: Implications for the opening of the Paleo-Tethys. *Lithos* (accepted paper LITHOS8253R2).

Tremblay, A., Meshi, A., Deschamps, T., Goulet, F., & Goulet, N. (2015). The Vardar Zone as a suture for the Mirdita ophiolites, Albania: constraints from the structural analysis of the Korabi-Pelagonia Zone. *Tectonics*, 34(2), 352-375.

Ustaömer, T., Robertson, A.H.F., Ustaömer, P. A., Gerdes, A., & Peytcheva, I. (2012a). Constraints on Variscan and Cimmerian magmatism and metamorphism in the Pontides (Yusufeli–Artvin area), NE Turkey from U–Pb dating and granite geochemistry. *Geological Society, London, Special Publications* doi: 10.1144/SP372.13.

Ustaömer, P. A., Ustaömer, T., Robertson, A. H. F. (2012b). Ion probe U-Pb dating of the central Sakarya basement: A peri-Gondwana terrane intruded by late lower Carboniferous subduction/collision-related granitic rocks. *Turkish Journal of Earth Sciences*, 21, 905–932.

Uto, K., Ishizuka, O., Matsumoto, A., Kamioka, H., & Togashi, S. (1997) Laser-heating $^{40}\text{Ar}/^{39}\text{Ar}$ dating system of the Geological Survey of Japan: System outline and preliminary results. *Bulletin of the Geological Survey of Japan*, 48, 23-46

Uzel, B., Langereis, C.G., Kaymakçı, N., Sözbilir, H., Özkaymak, Ç., & Özkaptan, M. (2015). Paleomagnetic evidence for an inverse rotation history of Western Anatolia during the exhumation of Menderes core Complex. *Earth and Planetary Science Letters*, 414, 108-125.

Van Hinsbergen, D.J.J., Torsvik, T.H., Schmid, S.M., Matenco, L.C., Maffione, M., Vissers, R.L.M., ... Spakman, W. (2019). Orogenic architecture of the Mediterranean region and kinematic reconstruction of its tectonic evolution since the Triassic. *Gondwana Research*, <https://doi.org/10.1016/j.gr.2019.07.009>

Vavassis, I., De Bono, A., Valloton, A., Stampfli, G.M., & Amelin, Y. (2000). U-P band Ar-Ar geo chronological data from Pelagonia basement in Evia (Greece): geodynamic implications for the Paleotethys subduction. *Schweizerische Mineralogische und Petrographische Mitteilungen*, 80,21–43.

Von Raumer, J.F., & Stampfli, G.M. (2008). The birth of the Rheic Ocean – Early subsidence patterns and subsequent tectonic plate scenarios. *Tectonophysics*, 461, 9-20.

Von Raumer, J., Bussy, F., Schaltegger, & Schulz, B. (2013) Pre-Mesozoic Alpine basements – Their place in the European Paleozoic framework. *Geological Society of America Bulletin*, 125 (1-2), 89-108.

Whitney, D.L., & Evans, B.W. (2010). Abbreviations for names of rock-forming minerals. *American Mineralogist*, 95 (1), 185–187.

Whitney, D.L., Teyssier, C., Kruckenberg, S.C., Morgan, V.L., & Iredale, L.J. (2008). High-pressure-low-temperature metamorphism of metasedimentary rocks, southern Menderes Massif, western Turkey. *Lithos*, 101, 218–232.

Wiedenbeck, M., Hanchar, J.M., Peck, W.H., Sylvester, P., Valley, J., White-house, M., ... Zheng, Y.F. (2004). Further characterization of the 91500 zircon crystal. *Geostandards & Geoanalytical Research*, 28:9–39.

Accepted Article

Wiederkehr, M., Sudo, M., Bousquet, R., Berger, A., & Schmid, S.M. (2009). Alpine orogenic evolution from subduction to collisional thermal overprint: the $^{40}\text{Ar}/^{39}\text{Ar}$ age constraints from the Valaisan Ocean, central Alps. *Tectonics*, 28, TC6009.

Wilke, F.D., O'Brien P., Gerdes, A., Timmerman, M. J., Sudo, M., & Khan, M.A. (2010). The multistage exhumation history of the Kaghan Valley UHP series, NW Himalaya, Pakistan from U-Pb and $^{40}\text{Ar}/^{39}\text{Ar}$ ages. *European Journal of Mineralogy*, 22, 703-719.

Wu, C.M., Wang, X.S., Yang, C.H., Geng, Z.S., & Liu, F.L. (2002). Empirical garnet-muscovite geothermometry in metapelites. *Lithos*, 62, 1-13.

Wu, C.M., & Zhao, G. (2006). Recalibration of the Garnet–Muscovite (GM) Geothermometer and the Garnet–Muscovite–Plagioclase–Quartz (GMPQ) Geobarometer for Metapelitic Assemblages. *Journal of Petrology*, 47(12), 2357-2368.

Zlatkin, O., Avigad, D., & Gerdes, A. (2017). The Pelagonian terrane of Greece in the peri-Gondwanan mosaic of the Eastern Mediterranean: Implications for the geological evolution of Avalonia. *Precambrian Research*, 290, 163-183.

SUPPORTING INFORMATION

Appendix S1. Sample preparation and analytical techniques.

Appendix S2. Ferrous iron determination.

Figure S1. (a) Normal and (b) inverse isochron diagrams for sample 12-123.

Table S1. $^{40}\text{Ar}/^{39}\text{Ar}$ geochronology data.

Table S2. Isotopic ratios resulting from Zr U-Pb geochronology (sample TR1620).

Table S3. Isotopic ratios resulting from LA-ICMPS geochronology (sample 112-1).

Table S4. Isotopic ratios resulting from LA-ICMPS geochronology (sample TR1610).

FIGURE CAPTIONS

FIGURE 1 (a) Map of the tectonic zones of the Hellenides (after Jacobshagen, 1986) and western Anatolia (Candan et al., 2016), (b) Red rectangles indicate the map areas of CBU located in western Anatolia, (c) Generalized geological map of the Cycladic Blueschist Unit in the Selçuk – Dilek area (after Candan et al., 2016). Diaspore / corundum-bearing metabauxite localities are marked (Candan et al., 1997).

FIGURE 2 Detailed geological maps and cross-sections of the CBU in Selçuk area.

FIGURE 3 Detailed geological maps and cross-sections of the CBU in (a) Tire, (b) Dilek Peninsula, (c) Gölarmara and (d) Gümüldür areas (after Başarır and Konuk (1981)). The rock unit explanations are given in Figure 2.

FIGURE 4 (a) Kyanite-chloritoid-phengite assemblage observed in pelitic layers of quartz metaconglomerate. The length of pencil is 15cm, (b) coherent series and tectonically overlying Selçuk mélange. Contact is a ductile thrust fault (NE of Selçuk), (c) Detailed geological map of a serpentinite block including eclogite and omphacite metagabbro bodies, N of Şirince, (d) Massive eclogite with secondary quartz veins and (e) omphacite metagabbro with fresh omphacite. Primary magmatic texture is partly preserved in statically recrystallized parts of the body. Cld: chloritoid, Czo: clinozoisite, Ed: edenite, Ep: epidote, Grt: garnet, Ky: kyanite, Omp: omphacite, Ph: phengite, Qz: quartz.

FIGURE 5 White mica compositions diagrams from the CBU: (a) muscovite (Ms) - paragonite (Pa) - celadonite (Cel); (b) Si vs (Mg+Fe²⁺) diagrams. The ideal celadonite - muscovite substitution line is shown as dotted line. (c-g) Amphibole compositions from the coherent series and the Selçuk mélange after Leake et al. (1997); (c) Na, (d,g) Na-Ca, (e,f) Ca-amphiboles.

FIGURE 6 Photomicrographs of high-P rocks from the CBU. (a) Kyanite – chloritoid - phengite assemblage from pelitic layers of quartz metaconglomerate, (b) kyanite porphyroblast replaced by pyrophyllite during greenschist overprint, (c) eclogite facies mineral assemblage composed of omphacite, epidote-I and euhedral garnet with omphacite and epidote-I inclusions, (d) replacement of omphacite by symplectite (Cpx-III + Ab) and Ca-amphibole formation related to decompression in eclogites, (e) omphacite-epidotite with weak foliation defined by parallel alignment of omphacite and epidote-I, (f) edenite crystals overgrowing symplectite, aggregates of (Cpx-II) and symplectite assemblage (Cpx-III+Ab) are derived from omphacite (Cpx-I), (g) glaucophane rimmed with barroisite and (h) resorption of garnet with albite corona in retrograded blueschist metabasites. Ab: albite, Brs: barroisite, Ca-amp: Ca-amphibole, Cld: chloritoid, Cpx: clinopyroxene, Czo: clinozoisite, Ed: edenite, Ep: epidote, Gln: glaucophane, Grt: garnet, Ky: kyanite, Ms: muscovite, Omp: omphacite, Ph: phengite, Prl: pyrophyllite, Qz: quartz.

FIGURE 7 (a) Representative clinopyroxene compositions of high-pressure blocks from the Selçuk mélange plotted on the Morimoto et al. (1988) diagram. (b) Chemical composition of garnets from the Selçuk mélange in a Fe²⁺+Mg-Ca-Mn ternary diagram.

FIGURE 8 (a) Compositional profiles and X-ray maps of garnet from (a-b) eclogite (SE-1), (c-d) blueschist metabasite (94-55/5) and (e) pelitic matrix of the Selçuk mélange (M98-99/2). The concentration of the element in X-ray maps increases from blue to red.

FIGURE 9 P-T pseudosections of the main rock types of the CBU calculated by Theriak-Domino software (de Capitani, 1994; de Capitani and Petrakakis, 2010) and the internally consistent, updated thermodynamic data set of Holland and Powell (1998) in the NCKFMASH (a-b) and NCFMASH (c-d-e-f) systems. Rock compositions used see Table 8. (a) Kyanite - chloritoid - phengite bearing quartz metaconglomerate from the coherent series, red line defines diaspore = corundum + H₂O reaction from Schmidt and Poli (1994), (b) Garnet phengite schist from the matrix of the Selçuk mélange, (c) Eclogite, (d) Omphacite metagabbro, (e) Omphacite

epidote and (f) Blueschist metabasite blocks from the matrix of the Selçuk mélange. Arrow shows stability field of the mineral.

FIGURE 10 (a-g) $^{40}\text{Ar}/^{39}\text{Ar}$ spectra of dating samples.

FIGURE 11 (a-b) Concordia diagram for zircon grains from eclogite (TR1620), zircon grains aged as (c) Carboniferous and (d) Triassic from TR1620, (e) zircon grain with Paleocene rim (56.2 ± 1.5 Ma) and Cretaceous core (85.9 ± 2.1 Ma), (f) Tera–Wasserburg diagram for allanite grains of garnet–phengite schist (112/1), (g-h-i) allanite crystals, used for age determination, showing parallel elongation to main foliation.

FIGURE 12 (a) Concordia diagram for monazite grains from quartz metaconglomerate (TR1610), (b) weighted average of $^{206}\text{Pb}/^{238}\text{U}$ apparent ages (TR1610), (c,d) monazite grains used in age determination.

FIGURE 13 (a) Upper Cretaceous (Cenomanian – Turonian) paleogeographical reconstruction indicating the relative positions of Pelagonian, Apulian and Anatolide-Tauride blocks which are separated by a transform fault zone. The future CBU in western Anatolia is marked by a red rectangle, (b) schematic SW-NE cross-section indicating northern (upper plate) and southern (lower plate) continental blocks which were separated by the Pindos Ocean, (c) early –middle Eocene (Ypresian – Lutetian) paleographic reconstruction indicating the relationship between the CBU and the MM, (d) early Eocene: cross-section indicating subduction-related epidote-blueschist and eclogite facies metamorphism in Selçuk mélange and oceanic crust, respectively, (e) middle Eocene: complete closure of Pindos Ocean, burial of the southern continental block, epidote-blueschist facies metamorphism of the coherent series. AM: Alanya Massif, BM: Bitlis Massif, CACC: Central Anatolia Crystalline Complex, CB: Cycladic Basement, CBU: Cycladic Blueschist Unit, Cp: Cyrenaica platform, ITS: Inner Tauride Suture, K: Kırşehir block, MM: Menderes Massif, Mp: Moesian platform, PABS: Pamphylian-Alanya-Bitlis Suture, Pm: Palmyra rift, Rd: Rhodope, Sk: Sakarya.

TABLE CAPTIONS

Table 1. Mineral assemblages of high-pressure rocks from coherent series and the Selçuk mélange.

Table 2a. Representative white mica analyses from coherent series and the Selçuk mélange.

Table 2b. Representative trioctahedral mica analyses from coherent series and the Selçuk mélange

Table 3. Representative epidote group minerals and chloritoid analyses from coherent series and the Selçuk mélange.

Table 4. Representative amphibole analyses from coherent series and the Selçuk mélange.

Table 5. Representative clinopyroxene analyses from high-pressure blocks in the Selçuk mélange.

Table 6. Representative microprobe analyses of garnet from the Selçuk mélange.

Table 7. P-T conditions for epidote - blueschist facies metamorphism and greenschist overprint obtained by conventional geothermobarometric calibrations and Theriak-Domino software from coherent series and the Selçuk mélange.

Table 8. Representative bulk rock compositions used for thermodynamic modelling.

Table 9. Descriptions of samples used in Ar-Ar and U-Pb age determinations.

Table 1. The general mineral assemblage of high-pressure rocks from coherent series and the Selçuk mélange

	coherent series		Selçuk mélange					
	1	2	3	4	5	6	7	8
Garnet			X			X	X	X
Clinopyroxene (I,II,III)			X	X	X			
Epidote	X	X	X	X	X	X		X
Clinozoisite	X	X	X	X	X	X	X	
Na amphibole		X				X		
Na-Ca amphibole		X			X	X		
Ca-amphibole		X	X	X	X	X		
Phengite	X	X					X	X
Biotite								X
Kyanite	X							
Chloritoid	X							
Chlorite	X	X	X			X	X	X
Pyrophyllite	X							
Albite		X	X		X	X	X	X
Quartz	X	X				X	X	X
Rutile			X		X			
Titanite		X	X		X	X	X	X
Calcite		X						
Apatite			X		X			
Opaque ox.	X	X			X	X	X	X

1) quartz metaconglomerate; 2) blueschist metabasite;

3) eclogite; 4) omphacite epidotite; 5) omphacite metagabbro;

6) blueschist metabasite; 7) garnet-phengite schist; 8) garnet-biotite schist

Table 2a. Representative white mica analyses from coherent series and the Selçuk mélange.

	Selçuk mélange						coherent series											
	metabasite		garnet-phengite schist				garnet-biotite schist				quartz metaconglomerate				blueschist metabasite			
	95-70/4	94-30	M98-99/2	M97-36	M99-52/5	D1	1*	2*	80/1	90/11								
SiO ₂	50.89	49.20	49.06	48.99	49.72	49.51	47.46	46.98	48.05	46.51	45.79	47.14	46.69	50.16	49.00	49.00	49.59	49.42
TiO ₂	0.14	0.33	0.58	0.24	0.02	0.27	0.39	0.38	0.40	0.39	0.00	0.16	0.03	0.42	0.13	0.17	0.12	0.25
Al ₂ O ₃	26.08	28.24	25.79	23.89	36.18	27.00	34.72	34.76	30.96	33.50	36.73	33.91	33.94	35.31	24.26	24.41	26.95	27.44
Fe ₂ O ₃	2.20	1.88	4.69	4.39	2.16	1.98	1.49	1.60	2.27	1.71	1.86	2.36	2.40	1.58	4.39	5.47	3.98	4.13
MnO	0.02	0.00	0.00	0.00	0.00	0.01	0.00	0.00	0.01	0.02	0.00	0.02	0.01	0.01	0.01	0.00	0.02	0.03
MgO	3.67	2.99	3.40	4.41	0.65	2.78	0.95	0.98	2.11	1.11	0.20	1.04	0.89	0.96	3.54	3.34	2.88	2.65
CaO	0.03	0.07	0.00	0.03	0.03	0.01	0.00	0.01	0.00	0.00	0.00	0.00	0.01	0.03	0.04	0.09	0.01	0.00
Na ₂ O	0.32	0.70	0.55	0.18	0.95	0.48	0.76	0.74	0.70	0.97	1.34	0.90	1.09	0.55	0.27	0.30	0.70	0.64
K ₂ O	10.67	9.63	10.43	10.93	9.03	8.91	7.62	9.04	9.43	9.00	9.05	9.87	10.01	8.39	9.92	9.54	10.11	10.22
Sum	94.02	93.07	94.49	93.06	94.43	94.02	93.37	94.48	93.94	93.24	94.95	95.40	95.08	97.41	91.65	92.37	94.43	94.85
Si	3.36	3.35	3.39	3.41	3.16	3.42	3.16	3.13	3.24	3.14	3.04	3.14	3.13	3.21	3.44	3.42	3.37	3.35
Ti	0.03	0.02	0.01	0.01	0.00	0.01	0.02	0.02	0.02	0.02	0.00	0.01	0.00	0.02	0.01	0.01	0.01	0.01
Al	2.08	2.26	2.19	1.96	2.71	2.20	2.73	2.73	2.46	2.67	2.88	2.66	2.68	2.66	2.01	2.01	2.16	2.19
Fe	0.27	0.11	0.13	0.26	0.11	0.11	0.08	0.09	0.13	0.10	0.10	0.13	0.13	0.08	0.26	0.32	0.23	0.23
Mn	0.00	0.00	0.00	0.00	0.00	0.00	0.00	0.00	0.00	0.00	0.00	0.00	0.00	0.00	0.00	0.00	0.00	0.00
Mg	0.35	0.30	0.33	0.46	0.06	0.29	0.09	0.10	0.21	0.11	0.02	0.10	0.09	0.09	0.37	0.35	0.29	0.27
Ca	0.00	0.01	0.00	0.00	0.00	0.00	0.00	0.00	0.00	0.00	0.00	0.00	0.00	0.00	0.01	0.00	0.00	
Na	0.07	0.09	0.05	0.02	0.12	0.06	0.10	0.10	0.09	0.13	0.17	0.12	0.14	0.07	0.04	0.04	0.09	0.08
K	0.91	0.84	0.87	0.97	0.73	0.79	0.65	0.77	0.81	0.78	0.77	0.84	0.86	0.68	0.89	0.85	0.88	0.88

Normalized to 22 oxygen, 1*=94-88, 2*=M97-135

Table 2b. Representative trioctahedral mica analyses from coherent series and the Selçuk melange

	Biotite											Chlorite						
	coherent series						Selçuk mélange					coherent series						
	garnet-biotite schist						1*		blueschist metabasite			garnet-mica schist				quartz metacong.		
	M97-36		M99-52/5				M98-24		52/2			M97-36		M99-52/5		M97-135	94-43/4	94-85/1
SiO ₂	36.79	36.56	37.72	36.91	37.03	37.60	37.51	37.36	38.52	27.64	27.79	24.77	26.18	22.70	23.58	26.99	27.87	26.70
TiO ₂	1.43	1.46	1.45	1.33	1.71	1.70	1.36	1.41	1.62	0.05	0.01	0.08	0.09	0.14	0.09	0.00	0.00	0.08
Al ₂ O ₃	17.70	17.75	17.53	17.89	18.66	18.12	17.22	17.56	14.87	19.89	20.22	22.07	21.80	21.10	22.08	24.41	22.88	23.24
Fe ₂ O ₃	18.05	19.29	17.06	18.47	16.75	17.13	17.35	17.49	14.97	15.59	17.00	24.74	21.92	29.58	32.30	6.90	8.24	9.77
MnO	0.05	0.11	0.02	0.14	0.08	0.06	0.03	0.04	0.65	0.87	0.92	0.12	0.08	0.20	0.19	0.95	0.85	1.20
MgO	11.03	10.33	11.65	10.05	10.08	10.45	11.77	11.35	14.37	23.16	21.95	14.84	17.86	10.52	9.16	24.55	23.73	23.08
CaO	0.04	0.00	0.04	0.08	0.02	0.10	0.05	0.03	0.09	0.00	0.01	0.07	0.00	0.00	0.00	0.01	0.00	0.00
Na ₂ O	0.10	0.05	0.12	0.05	0.08	0.02	0.15	0.18	0.05	0.00	0.04	0.02	0.00	0.06	0.02	0.02	0.01	0.02
K ₂ O	8.79	8.84	8.87	8.37	8.38	8.84	8.52	8.88	9.42	0.00	0.01	0.17	0.02	0.01	0.00	0.01	0.00	0.01
Sum	94.05	94.39	94.47	93.35	92.86	94.05	94.03	94.29	94.58	87.20	87.95	86.88	87.96	84.30	87.42	83.84	83.56	84.10
Si	5.61	5.59	5.68	5.66	5.65	5.68	5.68	5.66	5.79	2.79	2.80	2.63	2.69	2.57	2.60	2.69	2.80	2.70
Ti	0.16	0.17	0.16	0.15	0.20	0.19	0.16	0.16	0.18	0.00	0.00	0.01	0.01	0.01	0.01	0.00	0.00	0.01
Al	3.18	3.20	3.11	3.23	3.36	3.23	3.07	3.13	2.63	2.36	2.40	2.76	2.64	2.82	2.87	2.87	2.71	2.77
Fe	2.30	2.46	2.15	2.37	2.14	2.17	2.20	2.21	1.88	1.31	1.43	2.20	1.89	2.80	2.97	0.58	0.69	0.83
Mn	0.01	0.01	0.00	0.02	0.01	0.01	0.00	0.00	0.08	0.07	0.08	0.01	0.01	0.02	0.02	0.08	0.07	0.10
Mg	2.51	2.35	2.62	2.30	2.29	2.35	2.66	2.56	3.22	3.48	3.29	2.35	2.74	1.78	1.50	3.65	3.56	3.48
Ca	0.01	0.00	0.01	0.01	0.00	0.02	0.01	0.00	0.01	0.00	0.00	0.01	0.00	0.00	0.00	0.00	0.00	0.00
Na	0.03	0.01	0.04	0.01	0.02	0.01	0.04	0.05	0.01	0.00	0.01	0.00	0.00	0.01	0.00	0.00	0.00	0.00
K	1.71	1.72	1.70	1.64	1.63	1.70	1.65	1.71	1.81	0.00	0.00	0.02	0.00	0.00	0.00	0.00	0.00	0.00
Sum	15.51	15.52	15.47	15.40	15.30	15.36	15.47	15.50	15.62	10.03	10.01	9.99	9.98	10.01	9.97	9.88	9.84	9.91
X _{Mg}	0.52	0.49	0.55	0.49	0.52	0.52	0.55	0.54	0.63	0.71	0.69	0.52	0.59	0.39	0.33	0.85	0.82	0.79
Al ^{IV}	1.20	1.21	1.16	1.17	1.17	1.16	1.16	1.17	1.11	1.21	1.20	1.37	1.31	1.43	1.40	1.31	1.20	1.30
Al ^{VI}	0.39	0.39	0.40	0.45	0.50	0.46	0.38	0.40	0.21	1.15	1.20	1.39	1.34	1.39	1.46	1.56	1.52	1.48

Normalizations based on 22 oxygen for biotite, 14 oxygen for chlorite, 1*: garnet-mica schist, X_{Mg}=(Mg/Mg+Fe)

Table 3. Representative epidote group minerals and chloritoid analyses from coherent series and the Selçuk mélange

	epidote group minerals										chloritoid							
	Selçuk mélange										coherent series							
	eclogite		OE		BM		OM		BM		quartz metaconglomerate							
	SE-1	M97-151/3	94-55/5	52/2	91-16	90/11	80/1	M97-135/1	24/1	43/4	85/1							
	Czo	Czo	Czo	Czo	Czo	Czo	Ep	Czo	Ep	Ep	Czo	rim	inner r.	rim	core	inner r.	inner r.	inner r.
SiO ₂	38.24	39.16	38.77	39.11	38.44	38.41	37.90	38.81	37.65	38.40	37.90	25.09	25.20	25.11	24.69	25.20	25.06	25.12
TiO ₂	0.06	0.11	0.06	0.05	0.18	0.24	0.08	0.25	0.06	0.00	0.56	0.06	0.09	0.17	0.15	0.00	0.00	0.00
Al ₂ O ₃	25.32	27.47	26.03	27.73	26.32	26.31	21.51	27.82	22.60	23.38	26.85	41.13	41.01	41.03	40.41	42.00	41.10	42.17
Fe ₂ O ₃	8.55	7.12	8.78	6.73	7.74	8.29	13.62	5.98	12.57	11.73	6.57	11.51	12.16	12.95	13.33	11.16	12.81	11.78
MnO	0.42	0.32	0.30	0.27	0.42	0.63	0.80	0.13	1.30	0.02	0.18	5.91	3.48	4.00	4.82	4.45	3.09	4.12
MgO	0.03	0.06	0.07	0.08	0.04	0.06	0.01	0.09	0.06	0.05	0.10	7.33	8.60	7.72	7.05	8.57	8.19	8.02
CaO	22.40	23.92	23.55	23.62	23.12	23.16	22.44	23.43	21.94	23.39	23.72	0.01	0.01	0.00	0.00	0.00	0.00	0.00
Na ₂ O	0.00	0.00	0.00	0.03	0.00	0.00	0.01	0.08	0.01	0.03	0.02	0.04	0.04	0.02	0.02	0.01	0.00	0.02
K ₂ O	0.00	0.00	0.01	0.00	0.00	0.02	0.03	0.00	0.01	0.02	0.00	0.02	0.00	0.01	0.00	0.00	0.00	0.00
Cr ₂ O ₃	0.12	0.06	0.04	0.03	0.35	0.30	0.00	0.05	0.00	0.00	0.32							
Sum	95.14	98.23	97.61	97.66	96.61	97.41	96.40	96.64	96.21	97.02	96.23	91.10	90.59	91.00	90.46	91.39	90.25	91.23
Si	3.07	3.04	3.04	3.04	3.04	3.02	3.07	3.04	3.05	3.07	3.01	2.03	2.04	2.03	2.02	2.01	2.03	2.01
Ti	0.00	0.01	0.00	0.00	0.01	0.01	0.00	0.01	0.00	0.00	0.03	0.00	0.01	0.01	0.01	0.00	0.00	0.00
Al	2.40	2.51	2.41	2.54	2.45	2.44	2.06	2.57	2.16	2.20	2.51	3.93	3.90	3.92	3.90	3.94	3.93	3.98
Fe	0.52	0.42	0.52	0.39	0.46	0.49	0.83	0.35	0.77	0.70	0.39	0.07	0.10	0.08	0.10	0.06	0.07	0.02
Mn	0.03	0.02	0.02	0.02	0.03	0.04	0.06	0.01	0.09	0.00	0.01	0.71	0.73	0.79	0.81	0.68	0.80	0.76
Mg	0.00	0.01	0.01	0.01	0.00	0.01	0.00	0.01	0.01	0.01	0.01	0.41	0.24	0.27	0.33	0.30	0.21	0.28
Ca	1.93	1.99	1.98	1.97	1.96	1.95	1.95	1.97	1.91	2.00	2.02	0.44	0.51	0.46	0.43	0.51	0.49	0.48
Na	0.00	0.00	0.00	0.00	0.00	0.00	0.00	0.01	0.00	0.00	0.00	0.00	0.00	0.00	0.00	0.00	0.00	0.00
K	0.00	0.00	0.00	0.00	0.00	0.00	0.00	0.00	0.00	0.00	0.00	0.01	0.01	0.00	0.00	0.00	0.00	0.00
Cr	0.01	0.00	0.00	0.00	0.02	0.02	0.00	0.00	0.00	0.00	0.02	0.00	0.00	0.00	0.00	0.00	0.00	0.00
Sum	7.96	7.99	7.99	7.99	7.98	7.99	7.98	7.99	7.98	7.99	8.00	7.60	7.53	7.58	7.60	7.50	7.54	7.53
Ps	18	14	18	13	16	17	29	12	26	24	14							
Mg#												0.28	0.35	0.30	0.27	0.34	0.33	0.31

Normalizations based on 12.5 oxygen for epidote minerals, 12 oxygen for chloritoid, Mg#=[Mg/(Mg+Fe)],

Pistacite (Ps)=100*Fe³⁺/(Fe³⁺+Al), OE:omphacite-epidotite, BM: blueschist metabasite, OM: omphacite metagabbro

Table 4. Representative amphibole analyses from coherent series and the Selçuk mélange.

Sample no	coherent series											Selçuk mélange										
	Blueschist metabasite											Blueschist metabasite										
	90/11			80-1			T1			52-2			94-53-5			94-53-5						
	Na-Amp	Na-Ca Amp	Ca-Amp	Na-Amp	Na-Ca Amp	Ca-Amp	Na-Amp	Na-Ca Amp	Ca-Amp	Na-Amp	Na-Ca Amp	Ca-Amp	Na-Amp	Na-Ca Amp	Ca-Amp	Na-Amp	Na-Ca Amp	Ca-Amp				
SiO ₂	56.97	56.31	50.79	52.27	51.72	55.73	55.47	56.37	56.83	55.52	55.46	56.60	53.26	50.53	53.03	56.03	55.80	50.75	53.14	54.05	53.53	
TiO ₂	0.03	0.00	0.08	0.07	0.06	0.02	0.00	0.00	0.01	0.04	0.07	0.00	0.01	0.03	0.06	0.04	0.04	0.01	0.09	0.10	0.17	
Al ₂ O ₃	8.06	7.19	6.38	6.28	4.81	5.68	5.06	7.45	6.85	7.19	7.37	7.34	5.44	5.71	3.71	7.49	8.59	6.30	6.55	3.21	4.31	
Fe ₂ O ₃	15.10	15.70	17.15	16.86	15.37	13.70	14.79	15.12	15.93	14.18	14.38	15.44	12.98	14.84	11.38	15.30	13.48	15.33	15.00	10.93	10.87	
MnO	0.07	0.00	0.00	0.02	0.04	0.03	0.06	0.07	0.03	0.79	0.78	0.30	1.41	0.94	1.09	0.47	0.44	0.74	0.65	0.80	0.76	
MgO	9.89	10.06	12.23	11.42	13.53	11.44	11.45	10.43	10.24	11.05	11.09	10.43	14.07	13.70	16.52	9.90	10.26	12.46	11.46	16.74	15.97	
CaO	0.76	0.95	7.90	5.06	8.68	1.01	0.95	0.82	0.73	1.66	1.86	0.84	6.40	8.38	10.11	1.03	2.30	8.12	5.23	10.35	9.56	
Na ₂ O	6.88	6.88	3.52	5.06	2.84	7.03	7.19	7.25	7.12	6.12	6.08	6.70	3.89	2.59	1.50	6.97	6.44	2.80	5.14	1.80	2.53	
K ₂ O	0.03	0.01	0.20	0.15	0.16	0.01	0.02	0.03	0.01	0.03	0.04	0.02	0.11	0.19	0.09	0.02	0.04	0.21	0.13	0.16	0.18	
Cr ₂ O ₃	0.05	0.04	0.00	0.09	0.03	0.03	0.01	0.00	0.03	0.00	0.06	0.07	0.01	0.06	0.00	0.01	0.05	0.07	0.04	0.02	0.10	
Sum	97.84	97.13	98.25	97.28	97.24	94.69	95.00	97.54	97.78	96.57	97.18	97.73	97.58	96.97	97.49	97.27	97.44	96.79	97.43	98.15	97.97	
T: Si	7.88	7.88	7.26	7.47	7.43	7.96	7.93	7.85	7.90	7.76	7.71	7.83	7.47	7.22	7.45	7.84	7.81	7.31	7.58	7.58	7.54	
Al ^{IV}	0.12	0.12	0.74	0.53	0.57	0.04	0.07	0.15	0.10	0.24	0.29	0.17	0.53	0.78	0.55	0.16	0.19	0.69	0.42	0.42	0.46	
Fe ³⁺	0.00	0.00	0.00	0.00	0.00	0.00	0.00	0.00	0.00	0.00	0.00	0.00	0.00	0.00	0.00	0.00	0.00	0.00	0.00	0.00	0.00	
Ti	0.00	0.00	0.00	0.00	0.00	0.00	0.00	0.00	0.00	0.00	0.00	0.00	0.00	0.00	0.00	0.00	0.00	0.00	0.00	0.00	0.00	
T-Sum	8.00	8.00	8.00	8.00	8.00	8.00	8.00	8.00	8.00	8.00	8.00	8.00	8.00	8.00	8.00	8.00	8.00	8.00	8.00	8.00	8.00	
C:Al ^{VI}	1.20	1.06	0.34	0.53	0.24	0.92	0.78	1.07	1.02	0.94	0.92	1.02	0.37	0.18	0.18	1.08	1.22	0.38	0.68	0.11	0.25	
Ti	0.00	0.00	0.01	0.01	0.01	0.00	0.00	0.00	0.00	0.00	0.01	0.00	0.00	0.00	0.01	0.00	0.00	0.00	0.01	0.01	0.02	
Fe ³⁺	0.84	0.91	0.96	0.99	0.82	0.85	1.00	0.88	0.94	1.13	1.14	1.10	1.16	1.26	1.00	0.86	0.52	0.97	0.67	0.66	0.56	
Cr	0.01	0.00	0.00	0.01	0.00	0.00	0.00	0.00	0.00	0.00	0.01	0.01	0.00	0.01	0.00	0.00	0.01	0.01	0.00	0.00	0.01	
Mg	2.04	2.10	2.61	2.43	2.90	2.44	2.44	2.16	2.12	2.30	2.30	2.15	2.94	2.92	3.46	2.07	2.14	2.67	2.44	3.50	3.35	
Fe ²⁺	0.91	0.93	1.09	1.02	1.03	0.78	0.77	0.88	0.91	0.53	0.53	0.69	0.36	0.51	0.34	0.93	1.06	0.87	1.12	0.63	0.72	
Mn	0.01	0.00	0.00	0.00	0.00	0.00	0.01	0.01	0.00	0.09	0.09	0.04	0.17	0.11	0.13	0.06	0.05	0.09	0.08	0.09	0.09	
Ca	0.00	0.00	0.00	0.00	0.00	0.00	0.00	0.00	0.00	0.00	0.00	0.00	0.00	0.00	0.00	0.00	0.00	0.00	0.00	0.00	0.00	
C-Sum	5.00	5.00	5.00	5.00	5.00	5.00	5.00	5.00	5.00	5.00	5.00	5.00	5.00	5.00	5.00	5.00	5.00	5.00	5.00	5.00	5.00	
B:Ca	0.11	0.14	1.21	0.78	1.34	0.15	0.15	0.12	0.11	0.25	0.28	0.12	0.96	1.28	1.52	0.15	0.34	1.25	0.80	1.56	1.44	
Na	1.85	1.86	0.79	1.22	0.66	1.85	1.85	1.88	1.89	1.66	1.64	1.80	1.04	0.72	0.41	1.85	1.66	0.75	1.20	0.44	0.56	
B-Sum	1.96	2.00	2.00	2.00	2.00	2.00	2.00	2.00	2.00	1.91	1.92	1.92	2.00	2.00	1.93	2.00	2.00	2.00	2.00	2.00	2.00	
A:Ca	0.00	0.00	0.00	0.00	0.00	0.00	0.00	0.00	0.00	0.00	0.00	0.00	0.00	0.00	0.00	0.00	0.00	0.00	0.00	0.00	0.00	
Na	0.00	0.01	0.19	0.18	0.13	0.10	0.14	0.08	0.03	0.00	0.00	0.00	0.02	0.00	0.00	0.05	0.09	0.03	0.22	0.04	0.13	
K	0.00	0.00	0.04	0.03	0.03	0.00	0.00	0.00	0.00	0.00	0.01	0.00	0.02	0.03	0.02	0.00	0.01	0.04	0.02	0.03	0.03	
A-Sum	0.00	0.01	0.22	0.20	0.16	0.10	0.14	0.08	0.03	0.00	0.01	0.00	0.04	0.04	0.02	0.05	0.10	0.07	0.24	0.07	0.16	

Table 5. Representative clinopyroxene analyses from high-pressure blocks in the Selçuk mélange.

	eclogite						omphacite-epidotite						omphacite metagabbro					
	M98-45C			SE-I			M97-151/3			91-16			91-16			91-16		
	Cpx-I	Cpx-II	Cpx-III	Cpx-I	Cpx-I	Cpx-I	Cpx-I	Cpx-II	Cpx-III	Cpx-I	Cpx-I	Cpx-I	Cpx-II	Cpx-II	Cpx-III	Cpx-I	Cpx-II	Cpx-III
SiO ₂	56.22	55.93	54.38	53.23	55.22	54.93	56.10	55.53	55.58	54.54	56.38	56.43	55.88	55.68	53.61	54.12	54.12	54.12
TiO ₂	0.06	0.08	0.08	0.11	0.10	0.10	0.16	0.04	0.09	0.00	0.05	0.06	0.06	0.05	0.04	0.05	0.05	0.05
Al ₂ O ₃	11.42	11.24	6.91	2.33	2.74	9.58	8.29	9.76	8.82	8.24	3.06	10.47	10.20	7.61	7.76	5.18	5.75	5.75
Fe ₂ O ₃	5.17	5.53	6.37	7.09	6.98	5.47	7.44	5.64	8.63	9.85	3.31	3.46	3.24	3.47	11.95	8.86	8.86	8.86
MnO	0.05	0.03	0.11	0.22	0.17	0.79	0.54	0.28	0.32	0.25	0.12	0.13	0.21	0.18	0.41	0.74	0.74	0.74
MgO	7.12	7.25	9.97	12.13	12.64	8.54	8.65	8.77	7.28	10.72	8.80	8.92	10.87	10.73	8.28	9.30	9.30	9.30
CaO	12.31	12.93	16.63	21.45	22.24	13.85	14.63	12.14	14.25	18.07	13.04	13.79	15.99	15.82	15.86	16.25	16.25	16.25
Na ₂ O	7.92	7.45	5.28	2.28	1.79	6.74	6.03	7.66	6.31	7.25	4.06	7.44	7.06	5.68	5.41	5.29	5.29	5.29
K ₂ O	0.00	0.00	0.00	0.00	0.03	0.03	0.00	0.02	0.00	0.00	0.02	0.02	0.01	0.00	0.02	0.00	0.00	0.00
Cr ₂ O ₃	0.08	0.05	0.16	0.40	0.18	0.05	0.03	0.05	0.17	0.05	0.04	0.32	0.42	0.84	0.89	0.05	0.00	0.00
Sum	100.35	100.50	100.54	100.39	100.10	100.33	100.10	100.19	99.80	100.29	100.59	99.93	100.49	100.38	100.00	100.78	100.36	100.36
Si	1.98	1.98	1.97	1.98	1.96	1.97	1.99	1.99	1.99	1.99	1.99	1.99	1.99	1.98	1.95	1.96	1.96	1.96
Al ^{IV}	0.02	0.02	0.03	0.02	0.04	0.04	0.03	0.01	0.01	0.01	0.01	0.01	0.01	0.02	0.01	0.04	0.04	0.04
Sum	2.00	2.00	2.00	2.00	2.00	2.00	2.00	2.00	2.00	2.00	2.00	2.00	2.00	2.00	2.00	2.00	2.00	2.00
Al ^{VI}	0.46	0.45	0.26	0.09	0.08	0.36	0.40	0.36	0.34	0.12	0.42	0.41	0.30	0.31	0.17	0.20	0.20	0.20
Fe ²⁺	0.05	0.08	0.06	0.13	0.12	0.03	0.09	0.10	0.08	0.09	0.12	0.00	0.02	0.01	0.03	0.11	0.06	0.06
Fe ³⁺	0.10	0.08	0.13	0.09	0.09	0.14	0.12	0.13	0.08	0.17	0.18	0.09	0.08	0.11	0.07	0.25	0.21	0.21
Mg	0.37	0.38	0.53	0.66	0.69	0.45	0.46	0.36	0.46	0.39	0.58	0.46	0.47	0.57	0.45	0.50	0.50	0.50
Ti	0.00	0.00	0.00	0.00	0.00	0.00	0.00	0.00	0.00	0.00	0.00	0.00	0.00	0.00	0.00	0.00	0.00	0.00
Cr	0.00	0.00	0.00	0.01	0.01	0.00	0.00	0.00	0.00	0.00	0.01	0.01	0.01	0.02	0.03	0.00	0.00	0.00
Sum	0.99	1.00	0.99	0.98	0.99	0.98	1.00	1.00	0.99	1.00	0.99	0.99	1.00	1.00	0.99	0.98	0.98	0.98
Na	0.54	0.51	0.37	0.16	0.13	0.46	0.42	0.53	0.44	0.50	0.29	0.51	0.48	0.39	0.38	0.37	0.37	0.37
Ca	0.47	0.49	0.64	0.85	0.88	0.53	0.56	0.46	0.55	0.49	0.71	0.49	0.52	0.61	0.62	0.63	0.63	0.63
Mg	0.00	0.00	0.00	0.00	0.00	0.00	0.00	0.00	0.01	0.00	0.00	0.00	0.00	0.00	0.02	0.00	0.00	0.00
Sum	1.01	1.00	1.00	1.01	1.00	0.99	0.98	0.99	0.99	1.00	0.99	1.00	1.00	0.99	1.00	1.00	1.00	1.00
Quad	45	48	63	84	87	52	57	47	56	49	71	48	52	60	61	62	61	62
Jd	45	44	25	8	6	35	32	40	36	34	12	42	40	29	31	16	16	19
Ac	10	8	12	8	7	13	11	13	8	17	17	9	8	11	7	23	23	19
X _{Mg}	0.70	0.70	0.74	0.75	0.76	0.74	0.69	0.61	0.73	0.60	0.66	0.83	0.82	0.83	0.84	0.55	0.55	0.65

Normalized to 6 oxygens, X_{Mg}=(Mg/(Mg+Fe))

Table 6. Representative garnet analyses from the Selçuk mélange.

sample no	eclogite				blueschist metabasite				mélange schist			
	SE-1		M98-45C		52/2		94-55/5		M98-99/2		M98-90	
	c	r	r	c	r	c	r	c	r	c	r	c
SiO ₂	37.41	37.52	38.02	37.55	36.92	37.26	37.26	37.42	37.55	36.98	36.89	37.40
TiO ₂	0.10	0.07	0.16	0.16	0.06	0.16	0.07	0.13	0.09	0.15	0.07	0.07
Al ₂ O ₃	20.74	20.88	21.14	20.81	20.87	20.67	20.06	20.38	20.79	20.39	20.80	20.69
Fe ₂ O ₃	19.54	20.73	27.27	20.04	27.12	21.02	19.12	13.61	26.27	20.26	27.84	26.21
MnO	10.74	5.06	0.76	10.13	5.28	10.87	15.97	21.46	0.62	11.62	0.35	0.50
MgO	1.32	1.49	1.83	0.96	2.19	1.37	1.21	0.71	1.57	0.53	1.63	1.84
CaO	10.07	14.20	10.62	10.22	7.56	8.23	6.12	5.62	12.86	9.36	11.62	12.31
Na ₂ O	0.00	0.00	0.05	0.12	0.05	0.04	0.00	0.06	0.09	0.02	0.06	0.02
K ₂ O	0.00	0.00	0.00	0.03	0.01	0.02	0.00	0.01	0.00	0.01	0.01	0.01
Cr ₂ O ₃	0.05	0.01	0.08	0.04	0.00	0.09	0.09	0.06	0.03	0.10	0.03	0.09
Sum	99.97	99.96	99.92	100.05	100.06	99.73	99.90	99.47	99.86	99.41	99.29	99.13
Si	5.96	5.95	6.01	6.00	5.93	6.06	6.02	6.02	5.98	6.00	5.93	5.99
Ti	0.01	0.01	0.02	0.02	0.01	0.02	0.01	0.02	0.01	0.02	0.01	0.01
Al	3.93	3.90	3.95	3.93	3.95	3.80	3.88	3.86	3.90	3.90	3.94	3.91
Fe	2.63	2.77	3.63	2.69	3.64	2.81	2.57	1.83	3.50	2.75	3.74	3.51
Mn	1.45	0.67	0.10	1.37	0.72	1.58	2.18	3.09	0.08	1.60	0.05	0.07
Mg	0.33	0.35	0.46	0.22	0.52	0.32	0.29	0.17	0.37	0.13	0.39	0.44
Ca	1.73	2.44	1.81	1.75	1.30	1.40	1.08	1.02	2.19	1.63	2.00	2.11
Na	0.00	0.00	0.02	0.04	0.02	0.01	0.00	0.02	0.03	0.01	0.02	0.01
K	0.00	0.00	0.00	0.01	0.00	0.00	0.00	0.00	0.00	0.00	0.00	0.00
Cr	0.01	0.00	0.01	0.00	0.00	0.01	0.01	0.01	0.00	0.01	0.00	0.01
Sum	16.05	16.09	15.99	16.03	16.10	16.02	16.02	16.03	16.07	16.02	16.09	16.04
Alm(%)	42	42	60	44	58	45	41	29	56	44	59	56
Prp(%)	5	7	8	4	9	5	5	3	6	2	7	7
Sps(%)	24	11	2	23	12	26	36	51	2	27	1	1
Grs(%)	29	40	30	29	22	23	18	17	36	27	33	35

Normalized to 24 oxygen, r: rim, c: core

Table 7. P-T conditions for epidote - blueschist facies metamorphism and greenschist overprint obtained by conventional geothermobarometric calibrations and Theriak-Domino software from coherent series and the Selçuk mélange.

Geothermobarometric calibrations / Rock types	Coherent series				Selçuk mélange									
	Prograde		Retrograd		Prograde								Retrograde	
	T(°C)	P(kbar)	T(°C)	P(kbar)	T(°C) / P(kbar)								T(°C) / P(kbar)	
	Garnet-biotite schist	Blueschist metabasite	Garnet-biotite schist	Blue.meta./garnet-mica schist	Metapelitic matrix	Eclogite	Omphacite metagabbro	Omphacite epidotite	Blueschiste metabasite	Metapelitic matrix	Eclogite	Greenschist metabasite		
Green and Hellman (1982) Garnet-phengite	472-503 (14*)(15*)				503-540 (1*)(2*)						481-495 (1*)			
Wu et al. (2002) garnet-muscovite	491-521 (14*)(15*)		490-518 (14*)(15*)								511-560 (1*)			
Wu and Zhao (2006) garnet-muscovite											498-527 (1*)			
Williams and Grambling (1990) garnet-biotite			468-493(15*) 460-486(14*)											
Bhattacharya et al. (1992) garnet-biotite			471-483(15*) 479-497(14*)									479-496 (10*)		
Hodges and Sper (1982) garnet-biotite			452-471(15*) 470-485(14*)											
Ellis and Green (1979) garnet-clinopyroxene					531-617 (3,4,5,6*)			515-572 (8*)						
Krogh (1988) garnet-clinopyroxene					410-458 (3,4,5,6*)									
Graham and Powell (1984) garnet-amphibole									478-543 (9*)(10*)		490-545 (5*)			
Holland and Blundy (1994) amphibole-plagioclase											507-525 (13*)			
Holland (1980) jadeite-albite						14.5 ± 0.5 (4*)(16*)	14 ± 0.3 (7*)	14.2 ± 0.2 (8*)						
Kohn and Spear (1989) plg-hornb-grn-Qz												6 ± 1 (9*)(10*) 6.4 ± 0.5 (11*)		
Hodges and Crowley (1985) garnet - plagioclase - muscovite - biotite				5.9 - 7.6 (14*)(15*)										
Molina et al. (2015) plagioclase - amphibole		12 ± 2 (12*)		7 ± 0.5 (12*)										

Theriak-Domino	Coherent series		Selçuk mélange									
	quartz metacong.		metapelitic matrix		omphacite metagabbro		omphacite epidotite		blueschist metabasite		eclogite	
	Prograde	Retrograd	Prograde	Retrograd	Prograde	Retrograd	Prograde	Retrograd	Prograde	Retrograd	Prograde	Retrograd
	T(°C)	P(kbar)	T(°C)	P(kbar)	T(°C)	P(kbar)	T(°C)	P(kbar)	T(°C)	P(kbar)	T(°C)	P(kbar)
	490 ± 25 / 11.5 ± 1.5 kbar (17*)	410 ± 15 / 7 ± 1.5 kbar (17*)	520 ± 15 / 13 ± 1.5 kbar (18*)	510 ± 15 / 6 ± 1 kbar (18*)	515 ± 60 / 15 ± 3 kbar (19*)	485 ± 40 / 6-7 kbar (19*)	560 ± 40 / 16 ± 4 kbar (20*)	510 ± 30 / 6.5 ± 1.5 kbar (20*)	525 ± 35 / 13 ± 0.5 kbar (21*)	505 ± 15 / 6 ± 1 kbar (21*)	570 ± 30 / 18 ± 2 kbar (4*)	490 ± 30 / 6 ± 1 kbar (4*)

*(sample numbers)

1*(94-30),2*(M98-99/2) 3*(95-01), 4*(M98-45C),5*(95-21/10), 6*(SE-1), 7*(91-16), 8*(M97-151/3), 9*(94-55/5), 10*(52/2), 11*(M98-149/10), 12*(90/11), 13*(M97-31),14*(M97-36), 15*(M99-52/5), 16*(M99-5/4), 17*(D1), 18*(M98-99/2), 19*(M98-50/1), 20*(M98-151/3), 21*(52/2)

Table 8. Representative bulk rock compositions used for thermodynamic modelling

Sample	M98-99/2	M98-50/1	M97-151/3	M98-45C	52/2	D1
SiO ₂	64.85	47.31	47.06	48.73	47.36	64.60
TiO ₂	0.11	0.41	1.11	0.51	1.39	1.86
Al ₂ O ₃	16.51	16.45	15.06	14.54	13.73	17.80
FeO(t)	8.45	4.71	7.60	7.29	11.40	9.93
MnO	1.21	0.12	0.32	0.18	0.25	0.19
MgO	1.23	10.61	5.32	5.79	3.25	1.01
CaO	2.86	15.00	18.92	18.44	15.56	0.03
Na ₂ O	1.47	2.78	3.00	2.65	2.17	0.21
K ₂ O	3.06	0.1	<0.01	<0.01	0.05	1.84
P ₂ O ₅	0.00	0.02	0.02	0.58	0.17	1.62
H ₂ O	0.22	1.86	1.20	0.83	1.22	0.85
Sum	99.97	99.33	99.56	99.50	99.60	99.94

Table 9. Descriptions of the samples used in Ar-Ar and U-Pb age determinations.

	Ar-Ar white mica samples						Zr U-Pb samples			
	coherent series			contact	Selçuk mélange		c.s	Selçuk mélange		
	quartz metaconglomerate			garnet-biotite sch.		garnet-phengite schist		1*	2*	eclogite
	12-120/8	12-123	12-154/2	12-127/4	12-122/1	M98-100/3	12-142	TR-1610	112/1	TR-1620
Omphacite										X
Kyanite	X	X	X					X		
Chloritoid	X	X	X					X		
Phengite	X	X	X			X	X	X	X	
Epidote		X		X		X	X	X		X
Clinozoisite		X				X	X	X	X	
Garnet				X	X	X	X		X	X
Muscovite	X	X	X	X	X				X	
Biotite				X	X					
chlorite	X	X	X	X	X	X	X	X	X	
Plagioclase				X	X	X	X		X	
Pyrophyllite	X		X					X		
Rutile										X
Quartz				X	X	X	X		X	X
Opaque ox.	X	X	X			X		X		

1*:quartz metaconglomerate, 2*:garnet-phengite schist, c.s: coherent series

FIGURE 1a,b,c

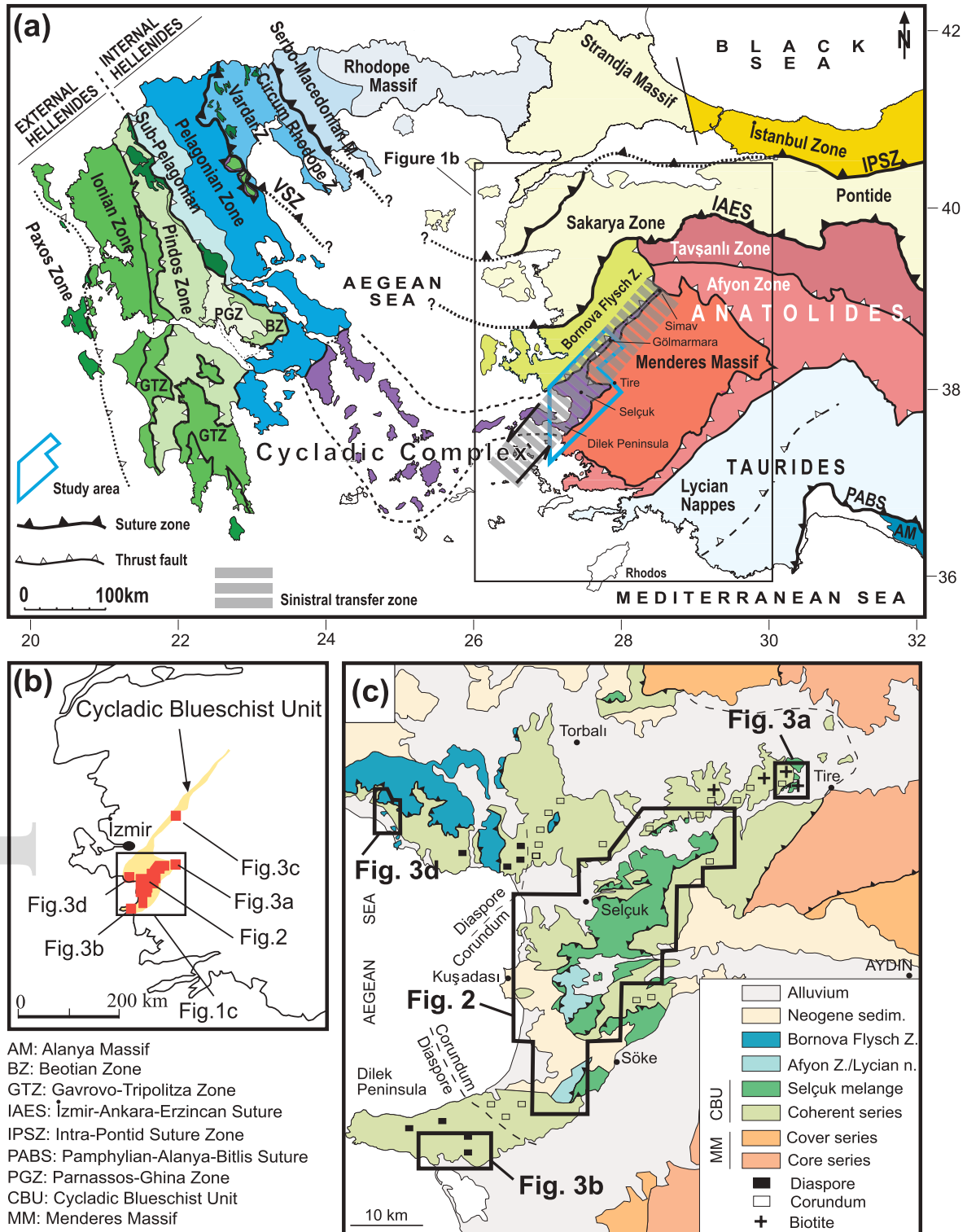


FIGURE 2

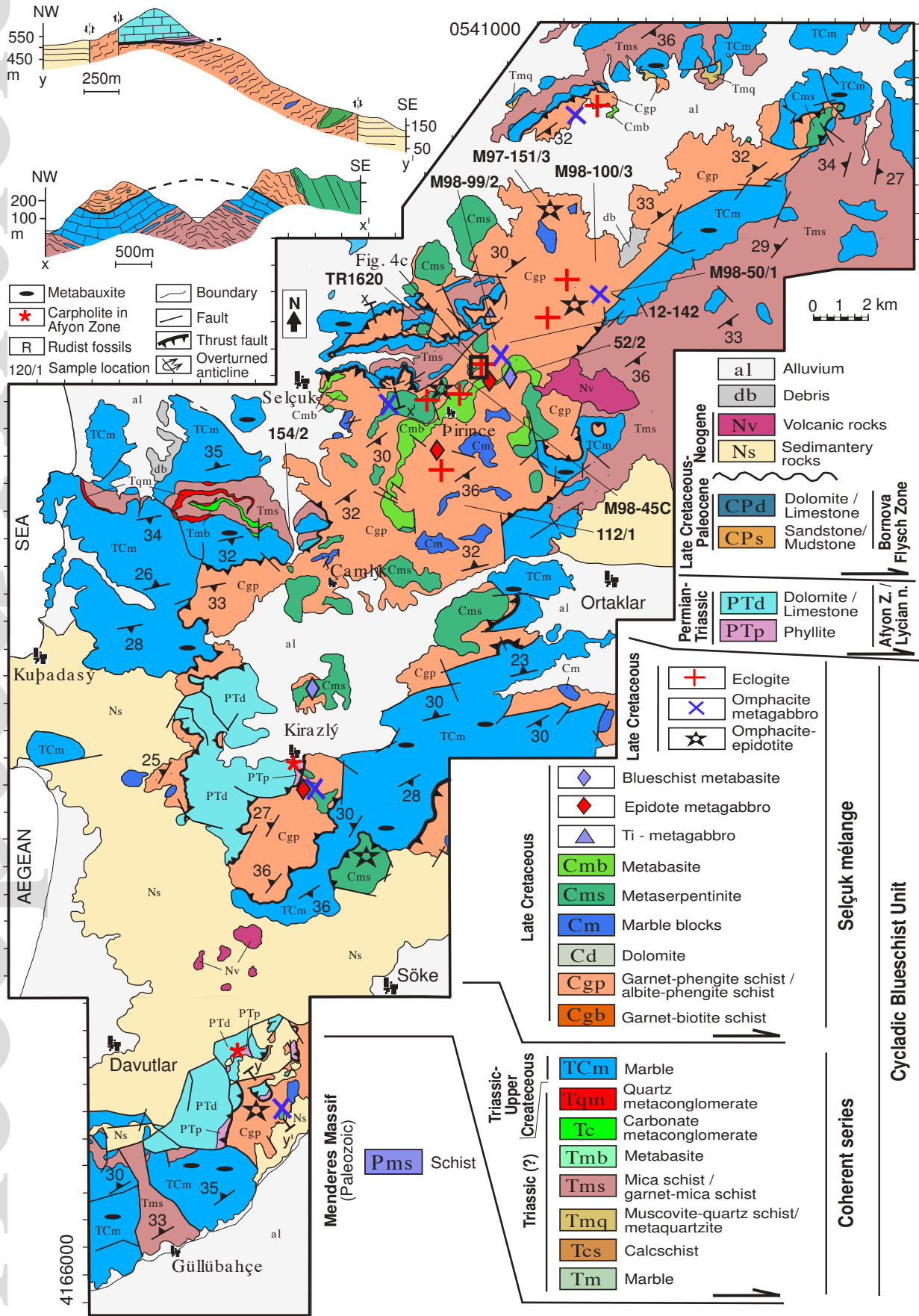


FIGURE 3a-b-c-d

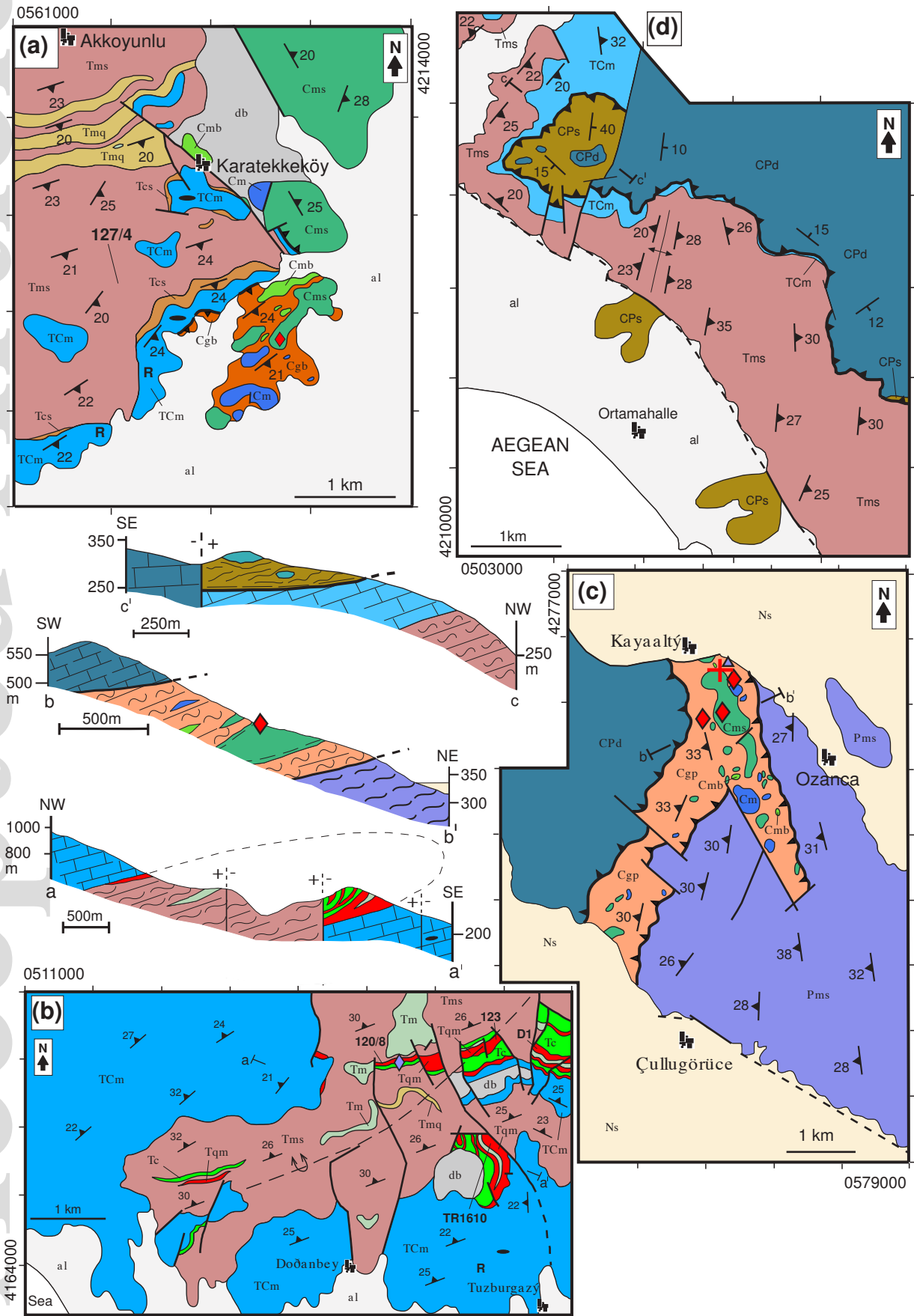


Figure 4a-b-c-d-e

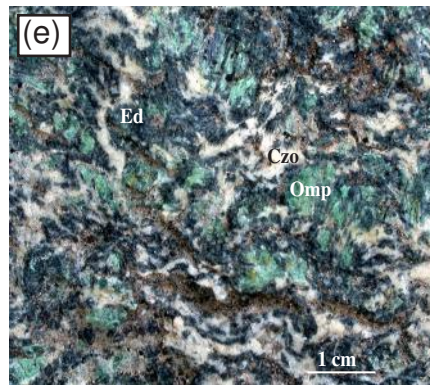
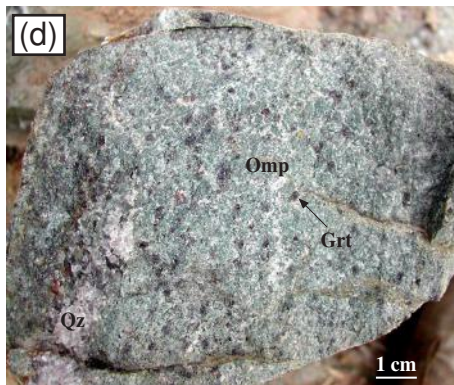
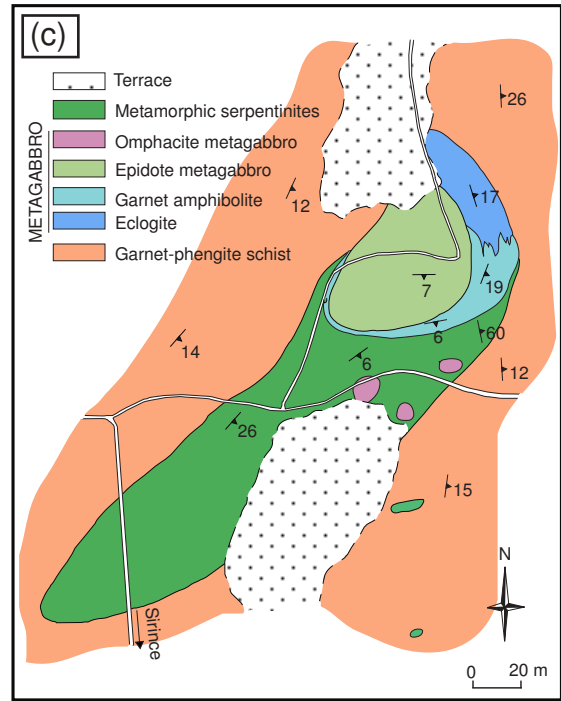
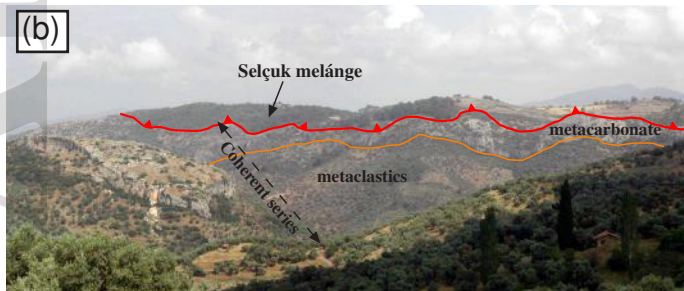
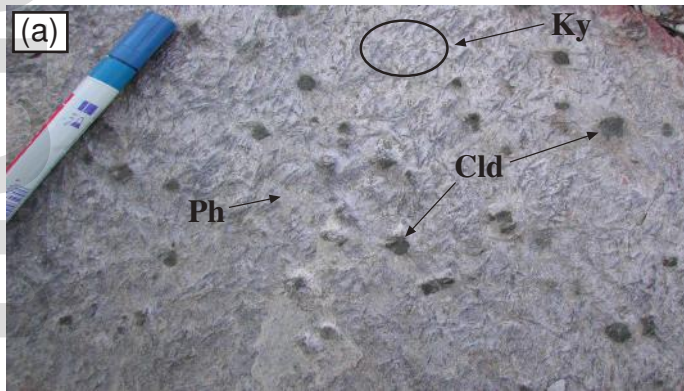


Figure 5a-b-c-d-e-f-g

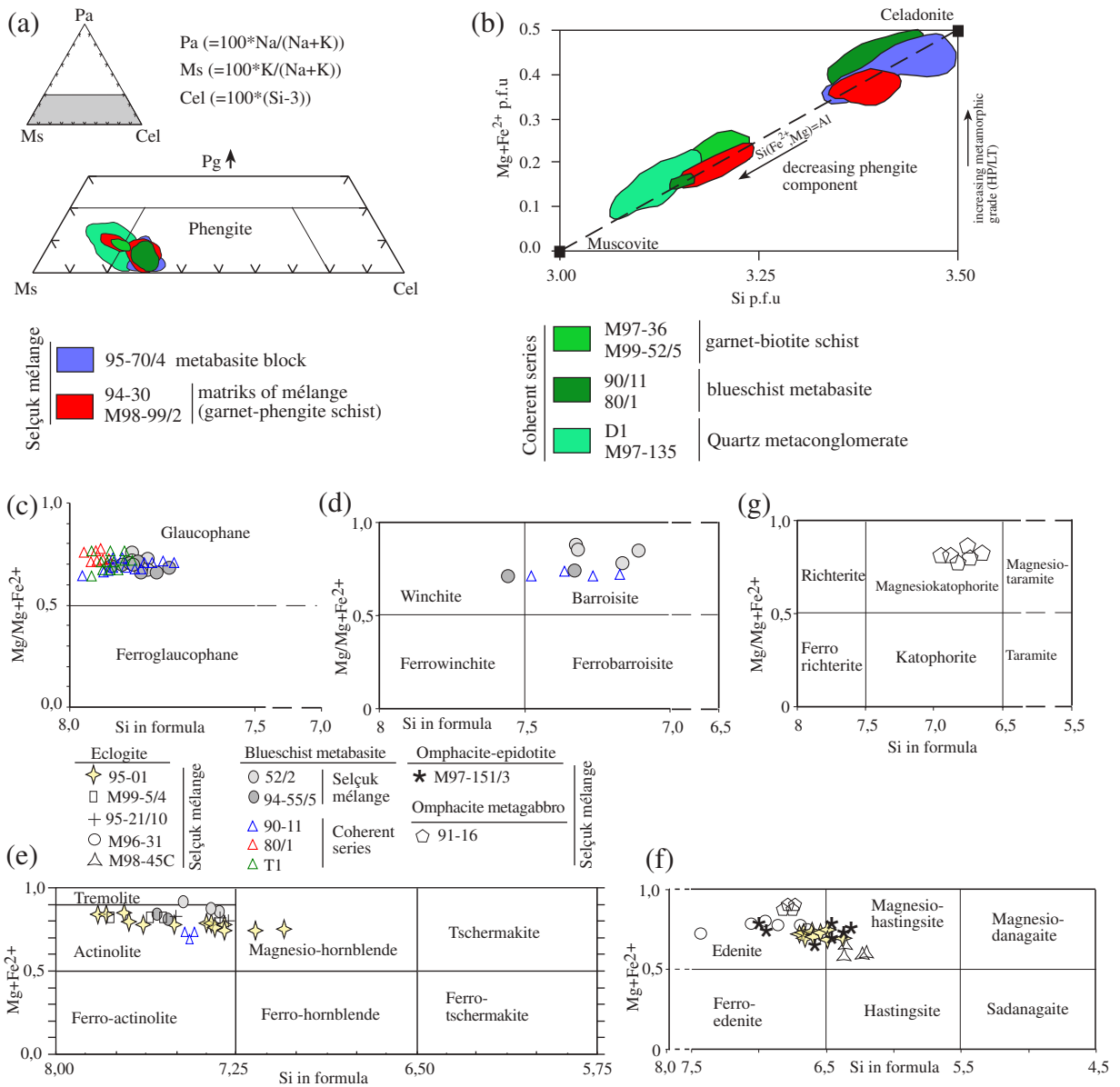


FIGURE 6a-b-c-d-e-f-g-h

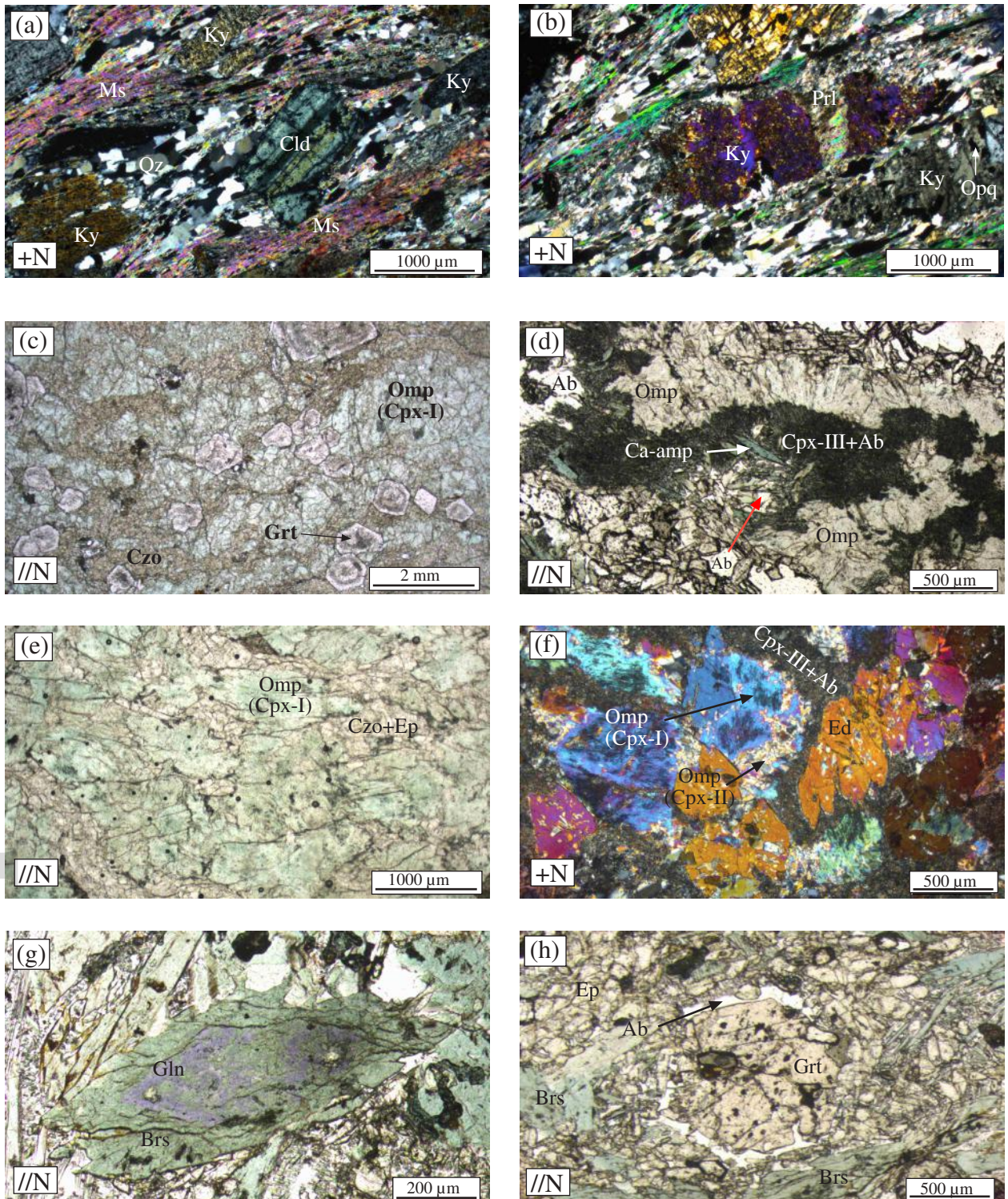


Figure 7a-b

Accepted Article

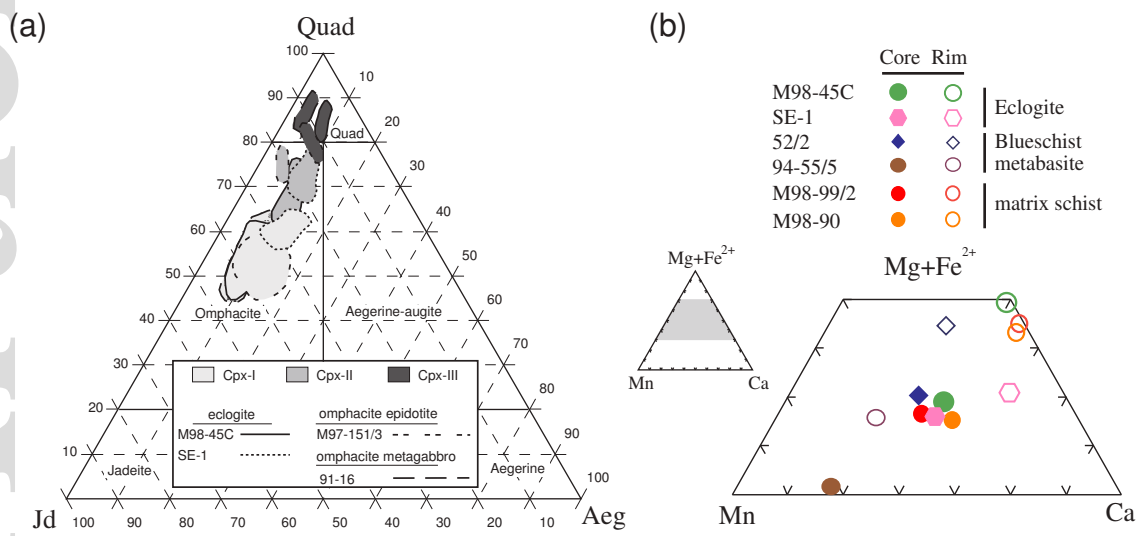


Figure 8a-b-c-d-e

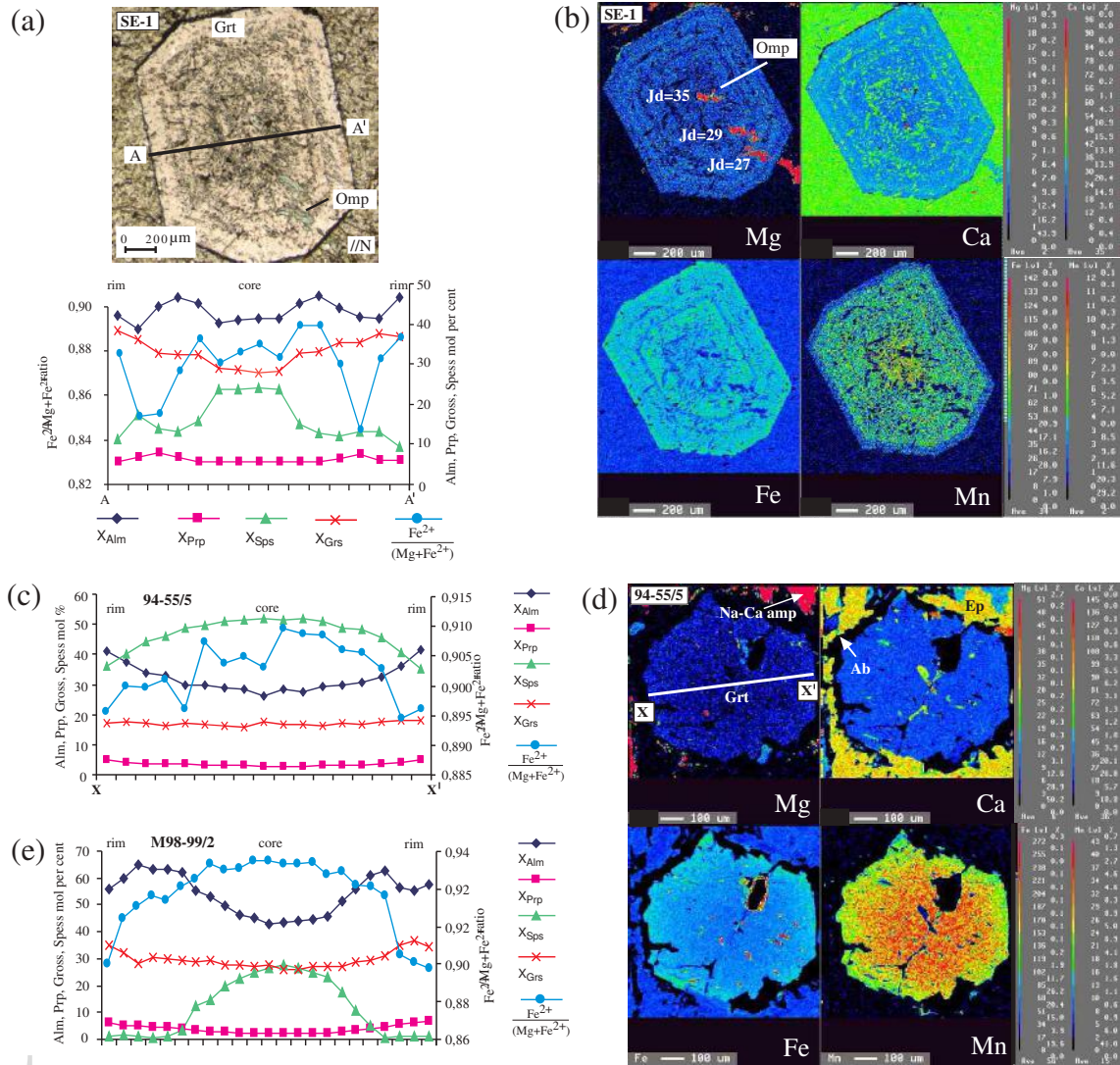


FIGURE 9a-b-c-d-e-f

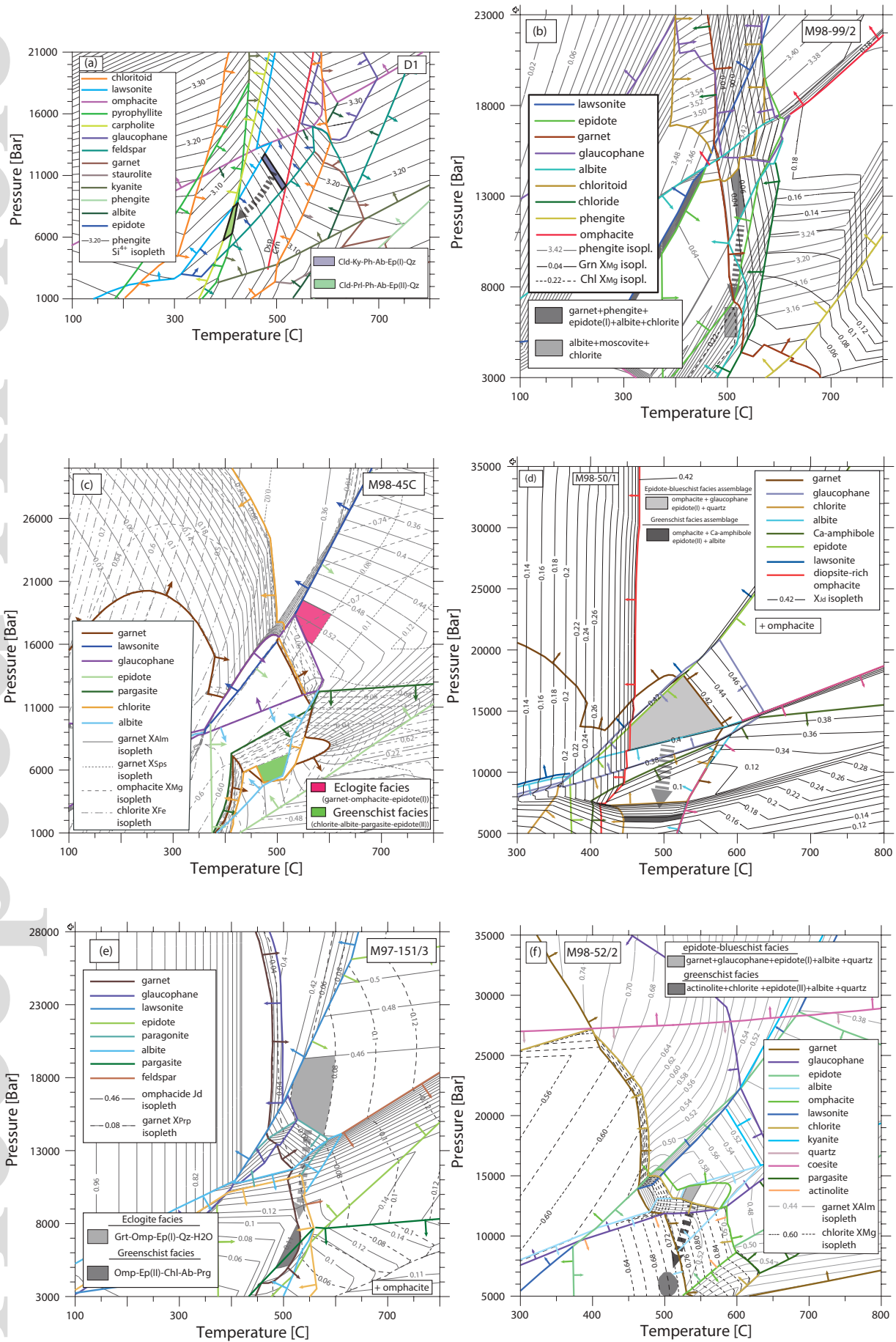


Figure 10a-b-c-d-e-f-g

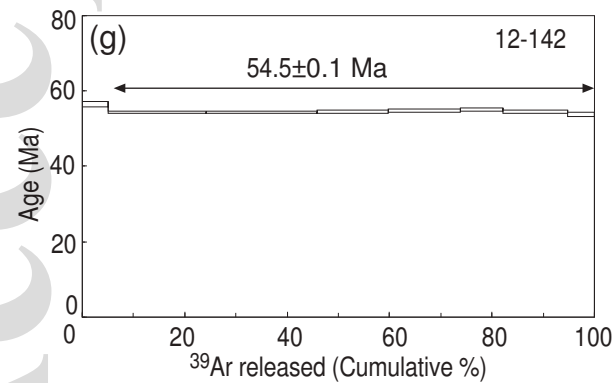
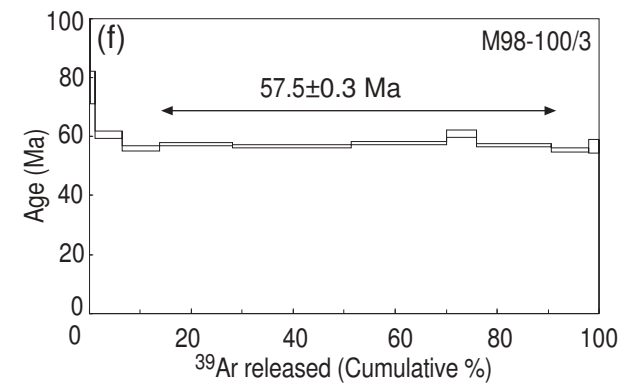
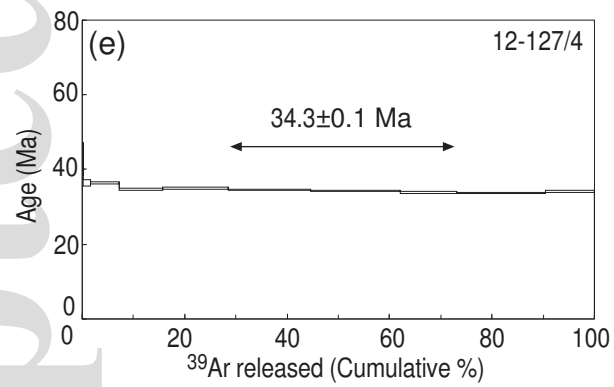
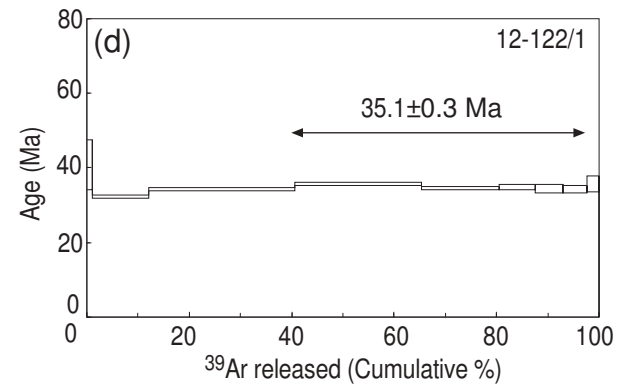
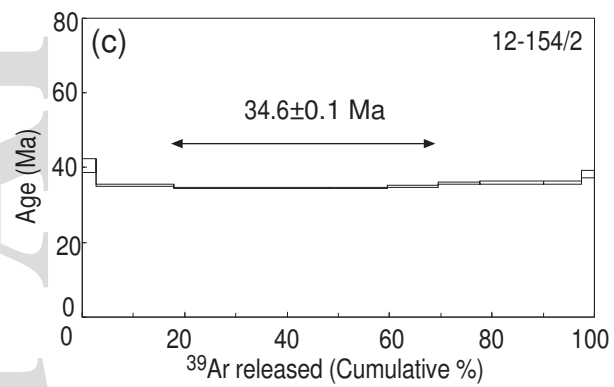
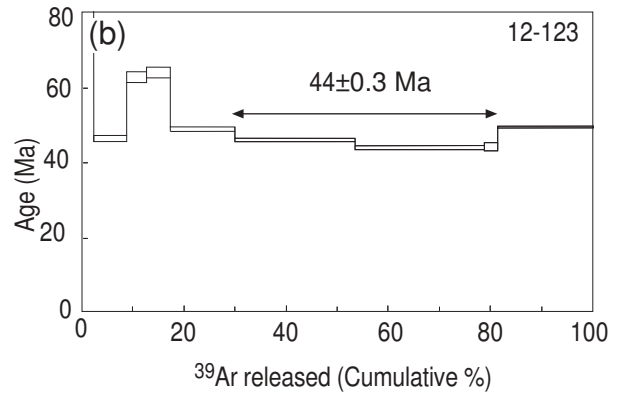
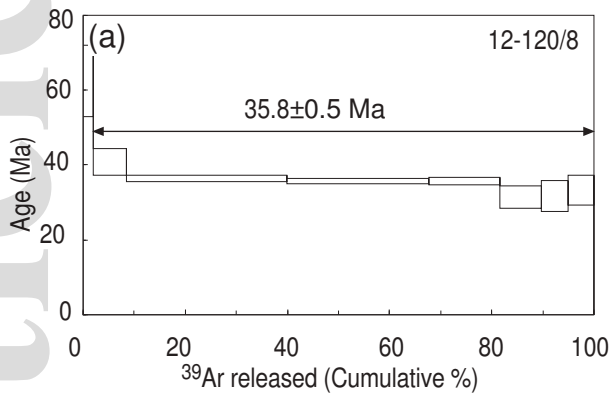


FIGURE 11a-b-c-d-e-f-g-h-i

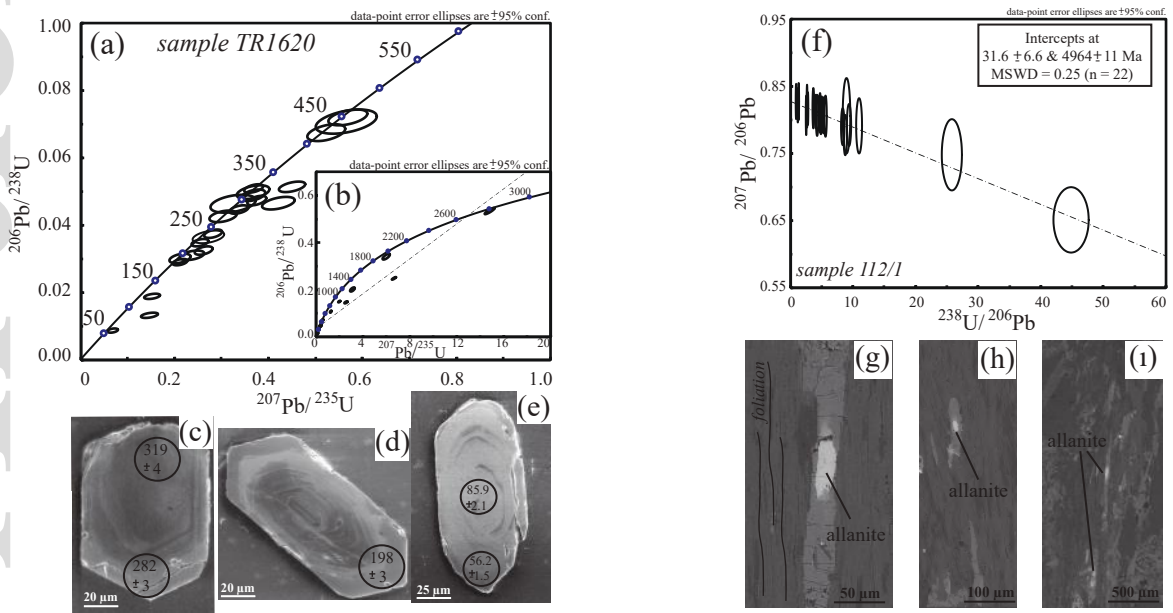
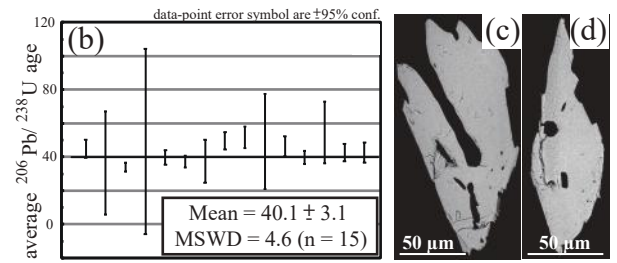
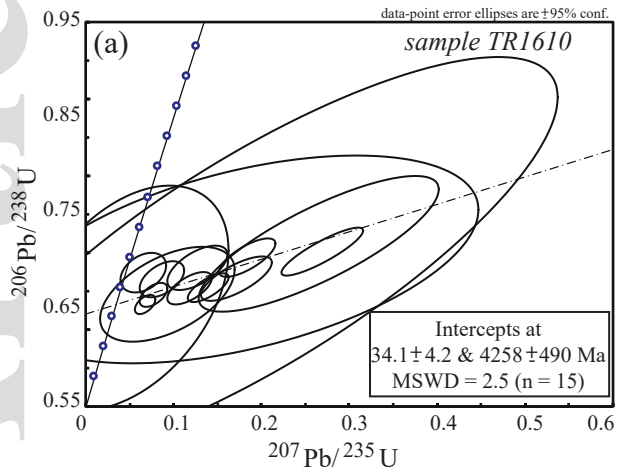


FIGURE 12a-b-c-d



ACCEPTED ARTICLE

Figure 13

